minerals

Article

Mineralogical Facies and Metal Enrichment in the Shallow-Water Hydrothermal System of Panarea Island (Aeolian Volcanic Arc, Mediterranean Sea)

Marcella Di Bella [1,*], Davide Romano [2], Valentina Volpi [1], Francesco Italiano [1], Giuseppe De Rosa [1], Alessandro Tripodo [3], Valentina Esposito [1], Teresa Romeo [4,5,6] and Giuseppe Sabatino [1,3]

[1] Istituto Nazionale di Oceanografia e di Geofisica Sperimentale–OGS, Borgo Grotta Gigante 42/C, Sgonico, 34010 Trieste, Italy; vvolpi@ogs.it (V.V.); fitaliano@ogs.it (F.I.); gderosa@ogs.it (G.D.R.); vesposito@ogs.it (V.E.); gsabatino@ogs.it (G.S.)
[2] Istituto Superiore per la Protezione e la Ricerca Ambientale–ISPRA, Via V. Brancati 48, 00144 Rome, Italy; davide.romano@isprambiente.it
[3] Dipartimento di Scienze Matematiche e Informatiche, Scienze Fisiche e Scienze della Terra–MIFT, Università degli studi di Messina, Viale Ferdinando Stagno d'Alcontres, 31, 98158 Messina, Italy; atripodo@unime.it
[4] Dipartimento di Biologia ed Evoluzione degli Organismi Marini, Stazione Zoologica Anton Dohrn, Sede Sicilia, Villa Pace, Contrada Porticatello 29, 98167 Messina, Italy; teresa.romeo@szn.it
[5] Istituto Superiore per la Protezione e la Ricerca Ambientale–ISPRA, Via dei Mille 46, 98057 Milazzo (ME), Italy
[6] National Biodiversity Future Center, NBFC, Piazza Marina 61, 90133 Palermo, Italy
* Correspondence: mdibella@ogs.it

Abstract

Shallow-water hydrothermal systems in active volcanic arcs serve as natural analogs for geothermal reservoir characterization and potential sources of Critical Raw Materials (CRMs). This study examines the Panarea hydrothermal system (Aeolian Islands, Tyrrhenian Sea, 37–207 m depth) to characterize its mineralogical facies and assess CRM enrichment patterns. Sixteen sediment samples collected during 2013–2015 research cruises were analyzed using SEM-EDS, XRPD with Rietveld refinement, and XRF. Four hydrothermal alteration facies were identified: (i) a low-temperature iron oxide facies dominated by nanocrystalline goethite with enrichments in As, V, and Mo; (ii) an argillic to propylitic facies containing smectite-group clays and high-temperature silica polymorphs, consistent with alteration at 200–350 °C; (iii) a phyllic to propylitic facies showing exceptional Ba enrichment (up to 46,976 ppm) and base-metal sulfide accumulations; and (iv) an advanced argillic facies including the first documented aluminophosphate–sulfate mineral at Panarea, a svanbergite–woodhouseite solid solution. Vanadium concentrations at Panarea exceed values reported across the Tyrrhenian–Aeolian domain, ranking this site among the highest-V shallow hydrothermal fields in the Mediterranean. These findings support a genetic model involving fault-controlled seawater circulation, magmatic CO_2 input, and episodic redox fluctuations, providing baseline data for CRM cycling and geothermal evaluation in Mediterranean submarine volcanic systems.

Keywords: iron oxyhydroxides; chimney-like structures; svanbergite–woodhouseite; hydrothermal vents; XRPD; SEM-EDS; XRF; Panarea island; Italy

Academic Editors: Pei Ni and Francisco J. González

Received: 12 March 2026
Revised: 30 April 2026
Accepted: 9 May 2026
Published: 11 May 2026

1. Introduction

https://doi.org/10.3390/min16050505

Submarine hydrothermal systems are critical natural laboratories where interactions among magmatic heat sources, circulating seawater, and reactive seafloor materials produce diverse mineral assemblages that influence local and global geochemical cycles [1–3]. These systems are characterized by high thermal gradients, chemically enriched vent fluids, and tectonic controls that create spatially heterogeneous zones of mineral precipitation, including sulfides, oxides, and silicates [4–6]. Beyond their fundamental scientific value for understanding ore-forming processes and biogeochemical element cycling, submarine hydrothermal systems have attracted growing attention as potential sources of economically strategic metals, including copper, zinc, cobalt, and rare earth elements, whose global demand is rapidly accelerating in the context of the clean energy transition [7,8].

The decarbonization pathways required to achieve net-zero emissions by mid-century rely heavily on renewable energy technologies, electric vehicles, and energy storage systems, all critically dependent on metals whose terrestrial reserves are under supply pressure [9–11]. This growing demand has intensified global interest in seafloor mineral resources, including seafloor massive sulfides (SMS), ferromanganese crusts, and polymetallic nodules, as potential complementary sources to conventional mining [8,12]. In the Mediterranean region, particularly within the Tyrrhenian Sea, hydrothermally derived metallic deposits associated with active volcanoes have been documented since the early 1990s [13–18], with massive sulfide accumulations enriched in Ba, Pb, and Zn; Fe–Si oxyhydroxide deposits; and iron-rich sediments highlighting the metallogenic potential of this geodynamically active basin [18,19]. However, exploitation of such resources raises profound environmental concerns, as seafloor hydrothermal ecosystems host unique and fragile chemosynthetic communities whose biodiversity and ecological functions remain poorly understood [20,21]. Any responsible resource assessment must therefore be grounded in rigorous scientific characterization of both geological and ecological dimensions so that future governance frameworks can balance resource extraction interests with the imperative to preserve marine biodiversity and ecosystem integrity [22,23].

In the Mediterranean region, particularly within the Aeolian volcanic arc and the central-southern Tyrrhenian Sea, submarine hydrothermal activity has been extensively documented, revealing significant mineralization, vigorous gas venting, and geochemical anomalies associated with active volcanic and tectonic processes [13,15–19,24]. The arc spans approximately 200 km from Calabria to the Sicilian shelf, encompassing seven islands (Alicudi, Filicudi, Salina, Lipari, Vulcano, Panarea, and Stromboli) and several submarine edifices. Its geological evolution is driven by the African–Eurasian plate convergence and Ionian slab rollback, which promote extensional tectonics, volcanism, crustal thinning, high heat flow (>150 mW/m^2), and widespread hydrothermal circulation [25–29]. Among the Aeolian Islands, the Panarea volcanic complex is notable for its shallow-water accessibility (37–207 m depth), vigorous degassing activity, and diverse mineralization styles [19,24,30,31]. The Black Point site (23 m depth) releases highly acidified (pH 2.4–3.3) thermal fluids at temperatures up to 140 °C [31,32], while the Smoking Land chimney-like structures field (70–80 m depth) releases CO_2-dominated gases with no apparent thermal anomalies [29,33]. Hydrothermal activity is expressed through Fe–Si oxyhydroxide chimney-like structures, mounds, flat deposits, sulfide mineralization, and iron-rich sediments forming distinctive yellow to red layers near active vents [29,33,34]. These shallow-water vents provide accessible analogs for understanding hydrothermal processes at deeper mid-ocean ridge and back-arc basin settings, offering insights into fluid–rock interaction, mineral precipitation kinetics, and microbial colonization [35–37]. Di Bella et al. [34] documented modern iron ooid deposits formed by hydrothermal precipitation of nanocrystalline goethite, demonstrating that direct inorganic precipitation can produce texturally and compositionally complex iron-rich structures under shallow submarine conditions.

Despite the geological significance of the Panarea hydrothermal field, a comprehensive integrated characterization across different deposit types remains limited. Previous studies have provided valuable, but fragmented, insights into specific mineral phases or bulk compositions, leaving gaps in our understanding of systematic phase assemblages, textural variations, and elemental distributions. This study addresses these gaps through integrated analysis of sixteen samples representing different hydrothermal deposits collected during 2013–2015 research cruises, including mobile seafloor sediments, sediment cores, and chimney fragments. We employ scanning electron microscopy with energy-dispersive X-ray spectroscopy (SEM-EDS) for textural and microchemical characterization, X-ray powder diffraction (XRPD) with Rietveld refinement for quantitative mineralogy, and X-ray fluorescence (XRF) spectrometry for bulk elemental analysis. The specific objectives are (1) to identify and quantify mineral assemblages across different deposit types and classify them within the established framework of hydrothermal alteration facies; (2) to characterize textural features, including evidence for biotic and abiotic precipitation processes; (3) to determine major and trace element distributions and enrichment patterns, with emphasis on EU-listed Critical Raw Materials; (4) to elucidate the spatial zonation of hydrothermal facies in relation to temperature, pH, and redox regimes, and (5) to provide baseline mineralogical and geochemical data to constrain metal cycling and hydrothermal dynamics in shallow submarine volcanic systems, with implications for predictive modeling of analogous deposits in volcanic arc settings.

1.1. Geological Setting

The Aeolian Arc (Figure 1a) represents the youngest phase of orogenic magmatism in the Tyrrhenian Sea, initiated approximately 23 Ma ago in response to the convergence of the African and Eurasian plates. The volcanic arc consists of seven islands (Alicudi, Filicudi, Salina, Vulcano, Lipari, Panarea, and Stromboli) and several seamounts (e.g., Sisifo, Enarete, Eolo, Alcione, and Palinuro) arranged in a predominantly submarine arcuate complex surrounding the Marsili basin, overlying a 250–300 km deep Wadati–Benioff zone related to the subduction of the Ionian Sea beneath the southern Tyrrhenian domain. Subaerial volcanic activity began around 250–270 ka; currently, only Stromboli is active, while Vulcano, Lipari, and Panarea are quiescent. Volcanic products belong to calc-alkaline, high-K calc-alkaline, shoshonitic, and K-alkaline series, reflecting mantle processes above the subducting oceanic crust [28,38]. The arc is located within an active region shaped by plate convergence and southeastward rollback of the Ionian lithosphere, generating compression in the eastern sector and strike-slip to extensional deformation in the central and western sectors [15,32]. The stratigraphic sequence spans basaltic to rhyolitic compositions dated from ~0.5 Ma to the present, with progressively younger rocks eastward [18,24]. The most prominent tectonic feature is the NNE–SSW to NE–SW trending graben northeast of Panarea, bounded to the west by extensional fault arrays with fresh volcanic outcrops, along which intense gas venting occurs. Adjacent sedimented areas display sulfide mineralization patches and iron-rich ochre to red sediments with consolidated iron oxide crust fragments [13,15,19]. Massive Ba–Pb–Zn-enriched sulfide deposits occur south of the Basiluzzo islet along the eastern fault zone [15–17].

Hydrothermal activity is expressed as Fe–Si oxyhydroxide chimneys, mounds, and extensive flat deposits, with widespread CO_2-dominated (92%–98%) seafloor gas discharges associated with variable H_2S and minor N_2, H_2, He, CO, and CH_4 [31,39]. Helium isotope ratios (4.1–4.3 Ra) indicate a strong mantle-derived component. Thermal waters have pH values of 3–7.45 and temperatures of 25–30 °C, are enriched in K^+, Ca^{2+}, Li^+, and Cl^-, and are depleted in Mg^{2+} and SO_4^{2-} relative to seawater [31]. Geothermal equilibrium temperatures estimated from fluid geochemistry range from 150 to 350 °C [31]; these represent deep subsurface thermal estimates and not direct measurements at the seafloor depths sampled here (37–207 m b.s.l.). In November 2002, a submarine gas explosion dramatically intensified hydrothermal activity, causing widespread seafloor disruption, the formation of new venting structures, and increased CO_2 flux and mineral precipitation [40,41]. The samples analyzed in this study were collected 10–13 years after this event (2013–2015) and may therefore reflect a post-disturbance recovery phase rather than long-term steady-state conditions, a temporal context that should be considered when interpreting the mineral assemblages and metal enrichment patterns described below.

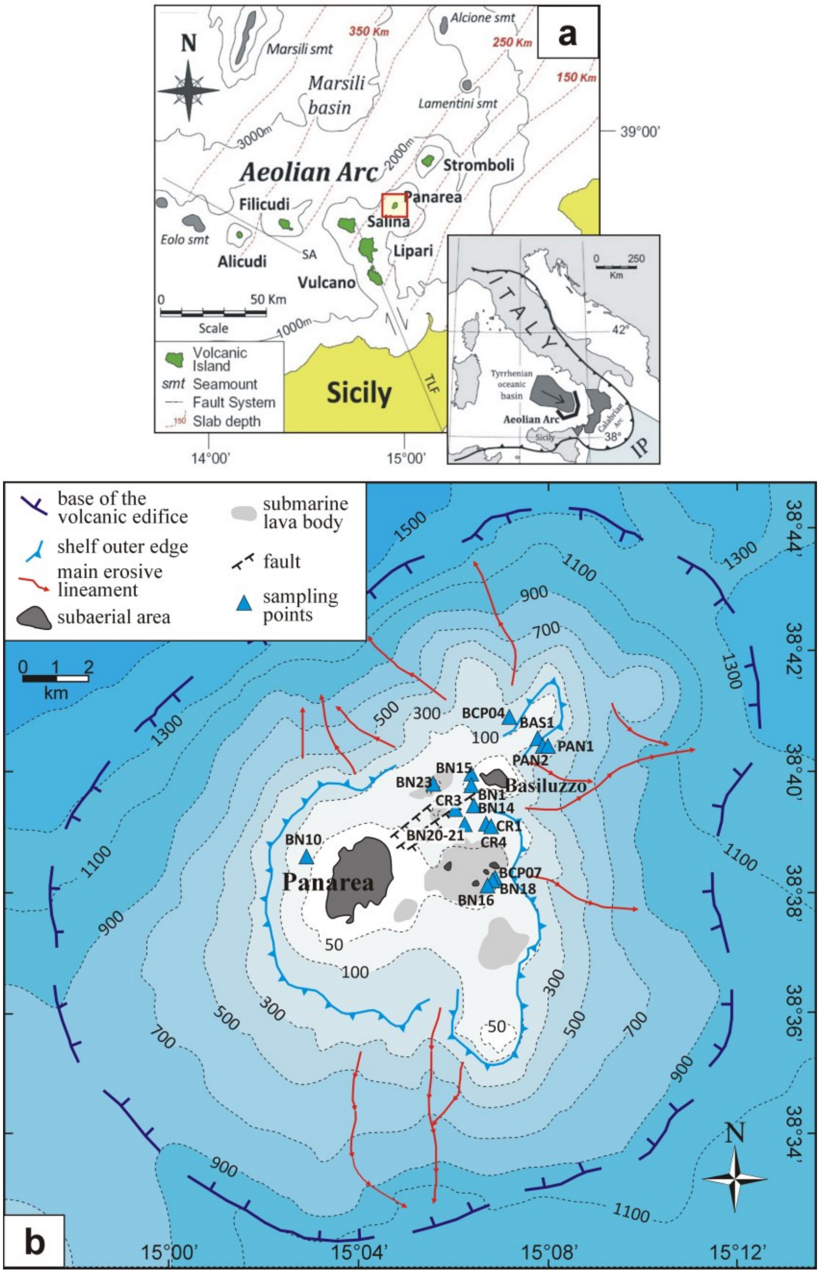

Figure 1. (**a**) Sketch map of the Aeolian Islands and surrounding seamounts in the southern Tyrrhenian Sea, modified from Peccerillo et al. [42], and location of the study area within the Panarea volcanic system (red square). The subduction/collision front is shown in the inset map of Italy. IP = Ionian Plate; SA = Sisifo–Alicudi fault system; smt = seamount; TLF = Tindari–Letojanni fault system. (**b**) Simplified bathymetric morphostructural map of the Panarea Volcanic Complex, modified from Lucchi et al. [43], showing sampling locations (blue triangles).

2. Materials and Methods

Sixteen shallow-water marine sediment samples (Figure S1; Table S1) were collected around Panarea Island during three research cruises: in 2013 aboard R/V Magnaghi and in 2014–2015 aboard R/V Astrea, coordinated by ISPRA in collaboration with other research institutions. Samples were recovered from depths ranging from 37 to 207 m below sea level (b.s.l.) in the area between Panarea Island and Basiluzzo Islet (Figure 1b). The sample suite includes distinct categories based on collection method and material type. Mobile seafloor sediments (BN1, BN10, BN14, BN16, BN18, BN21, BN23, BCP04, BCP07) and hydrothermal crusts (BAS1), consisting of sandy to gravel material with variable grain size and coloration, were collected using a bucket dredge. These sediments show variable degrees of hydrothermal alteration. Fragments of chimney-like structures, PAN1 and PAN2, were collected from two sites, both retrieved using a remotely operated vehicle (ROV). Three sediment cores (CR1, CR3, CR4) were obtained using a SW104 core drill to investigate vertical variations in hydrothermal precipitation and diagenetic alteration. The coordinates and water depths of all sampling stations are provided in Figure 1 and Table 1.

Table 1. Location, geographic coordinates, depth, and description of samples collected from the Panarea hydrothermal field.

Sample	Location	Latitude	Longitude	Depth (m b.s.l.)	Description
PAN1 *	NE Basiluzzo	15°07′46″ E	38°40′18″ N	184	red brown fragments of hydrothermal chimney, some with black patina
PAN2 *	NE Basiluzzo	15°07′50″ E	38°40′19″ N	207	red brown fragments of hydrothermal chimney, some with black patina
BN1 **	W Basiluzzo	15°06′14″ E	38°39′49″ N	86	red crusts
BN10 **	W Panarea	15°03′05″ E	38°38′23″ N	37	red crusts on coarse-grained sediment
BN14 **	SW Basiluzzo	15°06′15″ E	38°39′09″ N	81	grey brown sand
BN15 **	E Basiluzzo	15°06′15″ E	38°39′05″ N	81.5	red silty sand
BN16 **	S Lisca Bianca	15°06′51″ E	38°38′09″ N	74	brown sand with dispersed lithic clasts
BN18 **	S Lisca Bianca	15°06′52″ E	38°38′08″ N	74	red brown sand + crusts with black patina
BN21 **	SW Basiluzzo	15°05′60″ E	38°39′06″ N	75	grey green sand
BN23 **	W Basiluzzo	15°05′29″ E	38°39′36″ N	81	red, green coarse-grained sediment
BAS1 **	NE Basiluzzo	15°07′46″ E	38°40′21″ N	120	red brown crusts and sand
BCP04 **	NE Basiluzzo	15°07′07″E	38°40′40″N	87	red brown crusts and sand
BCP07 **	S Lisca Bianca	15°06′53″ E	38°38′09″N	74.8	Brown–red mound
CR1 ***	SSW Basiluzzo	15°06′29″ E	38°38′57″ N	87	core–red to brown sand
CR3 ***	SW Basiluzzo	15°05′52″ E	38°39′15″ N	82	core–grey to green mud with red patina
CR4 ***	SSW Basiluzzo	15°06′30″ E	38°38′55″ N	75	core–from brown to grey sand

Sampling method, date, and research vessel: * ROV–10/2015 Astrea; ** bucket–05/2014 (BCP4; BCP07), 10/2015, Astrea; *** corer–06/2013, Magnaghi.

The mineralogical and geochemical compositions of all samples were characterized using a multi-analytical approach that combined Scanning Electron Microscopy with Energy-Dispersive X-ray Spectroscopy (SEM-EDS) for microtextural and compositional analysis, X-ray Powder Diffraction (XRPD) for mineralogical phase identification, and X-ray Fluorescence (XRF) spectrometry for bulk major and trace element quantification:

- SEM-EDS–Microtextural characterization and semi-quantitative elemental analysis were performed with two electron microscopes: (1) the EMCrafts CUBE II Series (EmCrafts Co., Ltd., Gwangju-si, South Korea), equipped with a SE detector and 4CH BSE detector, located in the Panarea ECCSEL NatLab-Italy laboratory, managed by the National Institute of Oceanography and Applied Geophysics; and (2) the ESEM–FEI Inspect-S electron microscope (Thermo Fisher Scientific, headquartered in Hillsboro, OR, USA) coupled with the Oxford INCA PentaFETx3 EDX spectrometer and a Si(Li) detector, housed at the Department of Earth Sciences, University of Messina. The system is equipped with a Si(Li) detector with an ultra-thin window (ATW2), providing an energy resolution of 137 eV at 5.9 keV. Measurements were conducted under environmental conditions at a working distance of 10 mm with an acceleration voltage of 20 kV. Data acquisition used counting times of 60 s, maintaining approximately 3000 counts per second with dead time below 30%. Spectral processing and quantification were performed using INCA Energy software (version 4.09), which implements the XPP matrix correction scheme developed by Pouchou and Pichoir [44] to account for atomic number, absorption, and fluorescence effects.
- XRPD–Mineralogical phase identification was performed using a Bruker D8 ADVANCE diffractometer (Bruker AXS GmbH, Karlsruhe, Germany) equipped with Cu Kα radiation and a Bragg–Brentano theta-theta goniometer. The system includes a Si(Li) solid-state detector (Sol-X), which provides energy discrimination that substantially reduces iron-induced X-ray fluorescence and operates at 40 kV and 40 mA. Sample preparation procedures were adapted to the material type. Solid samples were manually pulverized with an agate mortar and dried in an oven at 37 °C. All samples recovered from the submarine environment, including dredged sediments, hydrothermal crusts, and sediment cores (CR1, CR3, CR4), were first washed with distilled water to remove soluble salt from seawater and interstitial pore fluids, then dried in an oven and pulverized. Diffraction patterns were collected from 2° to 80° 2θ with a step size of 0.02° 2θ and a count time of 1 s per step. Raw diffraction data were processed by filtering the Kα_2 component for all samples, exploiting the energy discrimination capability of the Sol-X solid-state detector, which substantially suppresses the Kα_2 contribution while retaining the full Kα_1 signal. For non-ferruginous samples, an additional background correction was performed using a digital (Fourier) filter, which improved the signal-to-noise ratio without loss of diagnostic information. For ferruginous samples, this additional digital background filtering was intentionally omitted: despite the energy discrimination of the Sol-X detector, residual background noise in these iron-rich samples remained elevated due to persistent Fe fluorescence, and digital filtering risked suppressing the weak, broad diffraction signals characteristic of nanocrystalline goethite. The Kα_2 stripping was therefore the only data pre-processing step applied uniformly across all samples prior to Rietveld refinement. Quantitative phase analysis was performed by Rietveld refinement using Profex 5.6.1 as a graphical interface to the BGMN engine, which implements a fundamental parameters approach for line-profile convolution from instrumental geometry and a dedicated instrumental file (.sav) describing the Bragg–Brentano θ-θ configuration with a Sol-X point detector. Refined parameters included scale factor, lattice constants, isotropic or anisotropic crystallite size (B1), microstrain (k2), and preferred orientation (SPHAR2/4) where required; background was modeled by

Chebyshev polynomial supplemented, for amorphous-rich samples, by dedicated amorphous structure files. Goodness-of-fit metrics (Rp, Rwp, Rexp, GoF, Durbin–Watson) for each refinement are reported in Supplementary Table S1.

- XRF–Bulk major and trace element compositions were determined using a Bruker S8 Tiger wavelength-dispersive sequential X-ray fluorescence spectrometer (Bruker AXS GmbH, Karlsruhe, Germany). The instrument features an Rh-anode X-ray tube capable of operating at a maximum power of 4 kW. For trace element analysis, measurements were performed at 60 kV and 67 mA using the LiF220 analyzer crystal with a 0.23° collimator, providing optimal peak-to-background ratios and spectral resolution for elements from Sc to U. To optimize signal-to-noise ratios and prevent detector saturation, tube voltage and current were adjusted according to the atomic number and concentration of each analyzed element. Sample preparation followed standardized procedures to ensure analytical reproducibility and minimize contamination. All samples were dried at 105 °C for 24 h and pulverized to a grain size of <63 μm using an agate mortar and pestle. Samples containing seawater were washed with distilled water prior to drying and pulverization to remove soluble salts that could interfere with matrix corrections. Homogenized powders were prepared using two methods: pressed pellets with boric acid binder for trace element analysis and fused glass beads prepared with lithium tetraborate flux in a Pt–Au crucible at 1050 °C for major element determinations. Loss on Ignition (LOI) was not determined; major element oxide concentrations are reported as measured, and analytical totals are included for reference only. All geochemical classifications rely on trace elements and REE patterns, which are insensitive to LOI normalization. Quantitative analysis was performed using the fundamental parameters method implemented in Bruker SPECTRA PLUS (version 3) software packages GEO-QUANT M (major and minor elements) and GEO-QUANT T (trace elements). The GEO-QUANT programs employ a hybrid empirical-fundamental parameters approach, with calibration curves based on international certified reference materials (CRMs) spanning diverse geological matrices. Matrix corrections are handled through the Compton scattering method (Rh Kα1 Compton line), with inter-element correction factors derived from fundamental physical constants (mass absorption coefficients, fluorescence yields, jump ratios). Certified reference material GBW07103 (Chinese marine sediment) was analyzed as an external standard to validate accuracy. Analytical precision, estimated from replicate analyses of standards, was better than 2% relative standard deviation (RSD) for major elements (>1 wt %) and 5%–10% RSD for trace elements in the 10–1000 ppm range. Lower limits of detection (LOD), calculated as 3σ of background intensity at optimized measurement times (Bruker Lab Report XRF 90, DOC-L80-E00090) [45], are reported in Tables 2–4; values below detection limits are reported as b.d.l. All XRF analyses were performed on bulk sample powders; element attribution to individual mineral phases is inferred from integration with XRPD quantitative mineralogy and SEM-EDS data.

Table 2. Major oxide contents (wt %) and trace element concentrations (ppm) in dredged marine sediments from Panarea Island, determined by XRF analysis.

Sample	BN1	BN10	BN14	BN15	BN16	BN18	BN20	BN21	BN23	BAS1	BCP04	BCP07
Major Oxides (wt %)												
SiO_2	13.51	4.15	58.82	11.36	55.17	55.98	71.51	70.46	48.13	9.98	12.86	57.49
Al_2O_3	3.71	1.34	16.55	2.48	11.56	11.32	13.47	13.95	9.05	2.18	1.27	25.65
Fe_2O_3	77.16	87.95	9.15	78.88	14.26	20.5	2.55	3.24	24.68	83.12	80.78	5.50
CaO	0.87	2.58	5.10	2.27	1.74	2.05	1.38	1.56	9.11	0.76	0.95	0.54
MgO	0.91	1.12	1.22	0.85	1.16	1.10	0.70	0.73	1.50	0.47	0.36	0.87

Na_2O		1.14	0.60	3.77	1.18	8.37	4.76	3.51	3.67	2.95	0.77	1.18	1.40
K_2O		0.85	0.20	3.85	0.88	4.19	1.79	5.71	5.26	3.10	0.42	0.61	0.55
TiO_2		0.13	0.52	0.54	0.027	0.317	0.52	0.20	0.23	0.22	0.10	0.08	1.88
P_2O_5		1.20	1.38	0.35	1.57	0.36	0.26	0.13	0.16	0.54	0.88	0.38	1.26
MnO		0.14	0.11	0.06	0.06	0.55	0.16	0.05	0.05	0.06	0.28	0.08	0.08
SO_3		0.32	0.40	0.46	0.40	1.94	1.35	0.67	0.58	0.54	0.42	0.81	4.49
Total		99.95	100.35	99.87	99.96	99.62	99.8	99.88	99.9	99.89	99.80	99.36	99.71
	LOD	Trace elements (ppm)											
Cd	~1 *	9	b.d.l.	b.d.l.	2	b.d.l.	b.d.l.	b.d.l.	b.d.l.	b.d.l.	b.d.l.	b.d.l.	b.d.l.
Sc	0.9	1	15	9	b.d.l.	6	16	2	2	5	b.d.l.	b.d.l.	16
V	1.2	1009	150	171	208	138	163	34	54	244	1030	291	180
Cr	1.0	46	21	28	8	12	29	13	11	36	33	12	37
Co	~1 *	b.d.l.	b.d.l.	4	b.d.l.	b.d.l.	b.d.l.	b.d.l.	b.d.l.	b.d.l.	b.d.l.	b.d.l.	5
Ni	0.7	70	8	8	31	17	13	9	9	16	61	35	11
Cu	0.8	31	30	32	26	32	35	23	24	33	45	29	54
Zn	0.5	132	131	86	159	80	179	50	53	101	160	64	57
Ga	~1 *	b.d.l.	18	19	b.d.l.	16	10	20	19	10	4	4	25
As	2.1	844	89	118	384	100	288	25	30	305	728	184	105
Rb	0.3	51	115	128	65	157	61	231	221	116	34	54	88
Sr	0.3	105	410	370	200	223	383	193	188	463	114	138	1320
Y	0.4	38	22	24	34	27	14	34	34	25	38	22	18
Zr	0.3	71	154	146	41	137	115	170	166	109	39	43	234
Nb	0.3	10	17	20	9	20	9	29	27	16	6	6	20
Mo	0.2	65	21	12	241	59	59	8	9	50	110	188	30
Ba	3.8	96	1066	538	44	390	965	446	327	398	90	74	980
La	3.4	<5	36	43	b.d.l.	44	8	65	63	22	12	12	35
Ce	3.8	38	53	71	77	75	31	105	100	71	31	31	24
Pb	0.9	69	147	70	195	118	168	42	47	78	45	30	289
Th	0.8	14	23	27	15	30	15	47	44	24	9	12	15
U	0.8	6	7	6	15	10	10	13	12	8	11	15	10

LOD = Lower limit of detection (3σ, Bruker Lab Report XRF 90, DOC-L80-E00090). b.d.l. = below detection limit. * = estimated from GEO-QUANT T specifications.

Table 3. Major oxide contents (wt %) and trace element concentrations (ppm) in PAN1 and PAN2 chimney-like structures from Panarea Island, determined by XRF analysis.

Sample		**PAN1**	**PAN2**	**PAN1_Replica**	**PAN2_Replica**
		Major Oxide (wt %)			
SiO_2		9.59	8.46	7.06	8.33
Al_2O_3		0.15	0.22	0.16	0.23
Fe_2O_3		85.39	86.49	87.67	85.94
CaO		0.77	0.66	0.72	0.63
MgO		0.36	0.44	0.43	0.46
Na_2O		2.37	2.28	2.30	2.91
K_2O		0.24	0.22	0.21	0.25
TiO_2		0.00	0.00	0.01	0.01
P_2O_5		0.06	0.05	0.06	0.04
MnO		0.90	0.85	0.40	0.38
SO_3		1.03	1.17	1.39	1.17
Total		100.86	100.84	100.40	100.37
	LOD	Trace elements (ppm)			

Cd	~1 *	b.d.l.	b.d.l.	b.d.l.	b.d.l.
Sc	0.9	b.d.l.	b.d.l.	b.d.l.	b.d.l.
V	1.2	99	88	69	66
Cr	1.0	b.d.l.	b.d.l.	b.d.l.	b.d.l.
Co	~1 *	b.d.l.	b.d.l.	b.d.l.	b.d.l.
Ni	0.7	38	50	19	38
Cu	0.8	40	28	28	30
Zn	0.5	41	48	61	65
Ga	~1 *	4	4	4	4
As	2.1	65	50	39	35
Rb	0.3	11	13	14	16
Sr	0.3	120	104	85	95
Y	0.4	41	11	8	9
Zr	0.3	b.d.l.	b.d.l.	b.d.l.	1
Nb	0.3	3	2	1	1
Mo	0.2	171	199	255	249
Ba	3.8	32	22	20	14
La	3.4	12	12	12	12
Ce	3.8	11	1	1	1
Pb	0.9	11	8	10	10
Th	0.8	3	3	3	2
U	0.8	12	18	19	19

LOD = Lower limit of detection (3σ). b.d.l. = below detection limit. * = estimated.

Table 4. Major oxide contents (wt %) and trace element concentrations (ppm) in core samples from Panarea Island, determined by XRF analysis.

Sample		**CR1 0–3**	**CR1 3–9**	**CR1 18–21**	**CR1 21–24**	**CR1 24–27**	**CR1 27–30**	**CR1 30–37**	**CR3 0–3**	**CR3 3–12**	**CR4**
					Major Oxide (wt %)						
SiO_2		68.27	82.59	74.18	81.60	52.90	73.61	78.03	61.66	64.00	58.70
Al_2O_3		10.30	6.91	8.15	8.20	25.33	13.22	11.09	16.62	17.24	22.00
Fe_2O_3		4.72	1.70	2.43	1.74	5.36	2.60	2.42	4.86	4.54	6.02
CaO		2.22	1.06	1.83	1.04	0.33	2.20	1.55	3.25	3.84	1.54
MgO		0.80	0.67	1.52	0.53	2.35	0.58	0.48	0.99	0.89	2.30
Na_2O		2.25	1.47	2.63	1.29	2.62	2.08	1.96	5.45	2.63	1.41
K_2O		1.33	0.51	1.19	0.81	0.51	2.39	2.24	3.87	4.03	1.43
TiO_2		0.78	1.40	1.09	0.90	1.26	0.60	0.59	0.59	0.56	1.03
P_2O_5		0.15	0.09	0.15	0.23	0.13	0.16	0.14	0.30	0.30	0.19
MnO		0.01	0.01	0.01	0.01	0.01	0.03	0.04	0.03	0.06	0.13
SO_3		10.03	3.14	5.72	3.61	7.80	2.52	1.51	0.74	0.38	3.72
Total		100.86	99.55	98.90	99.96	98.60	99.98	100.05	98.36	98.47	98.47
	LOD					Trace elements (ppm)					
Cd	~1 *	b.d.l.	b.d.l.	b.d.l.	b.d.l.	b.d.l.	b.d.l.	b.d.l.	b.d.l.	b.d.l.	b.d.l.
Sc	0.9	12	9	7	10	42	13	9	17	14	39
V	1.2	90	76	79	98	205	135	114	171	162	257
Cr	1.0	10	11	12	8	44	4	13	36	32	49
Co	~1 *	b.d.l.	b.d.l.	b.d.l.	b.d.l.	6	b.d.l.	b.d.l.	2	4	7
Ni	0.7	5	9	b.d.l.	4	13	6	12	12	9	14
Cu	0.8	38	19	27	28	68	30	27	33	33	79
Zn	0.5	63	23	46	41	1265	40	41	331	362	1920
Ga	~1 *	16	12	12	13	26	16	17	19	19	23

As	2.1	59	47	60	36	251	60	58	132	96	150
Rb	0.3	22	9	18	17	12	83	99	110	125	32
Sr	0.3	2114	791	1467	1485	762	1223	775	474	434	1197
Y	0.4	16	18	16	10	15	19	19	19	20	23
Zr	0.3	351	351	379	230	228	264	247	137	138	269
Nb	0.3	14	22	19	14	17	17	19	15	16	14
Mo	0.2	21	27	31	23	34	30	27	23	13	42
Ba	3.8	46,976	12,753	26,738	19,091	1109	26,174	11,710	2021	1535	13,234
La	3.4	<5	7	<5	6	42	<5	19	29	44	15
Ce	3.8	<5	<5	<5	<5	62	<5	<5	26	35	<5
Pb	0.9	209	81	135	282	407	137	99	244	292	400
Th	0.8	11	10	10	11	16	18	22	19	23	14
U	0.8	8	8	8	8	7	9	8	9	8	9

LOD = Lower limit of detection (3σ). b.d.l. = below detection limit. * = estimated.

3. Results

The hydrothermal sediments collected from the Panarea volcanic field were characterized using SEM imaging, X-ray diffraction, and geochemical analyses. The following subsections present the results organized by analytical approach: textural characterization, mineralogical assemblages, major element geochemistry and sample classification, and trace element signatures. Together, these data document the compositional and textural diversity of the sampled materials, which include ferruginous crusts, silica-dominated sediments, chimney fragments, and sediment cores.

3.1. Textural Characterization of Hydrothermal Sediments

SEM imaging reveals a range of textures reflecting the mineralogical and compositional diversity of the Panarea hydrothermal sediments (Figure 2). Iron-rich crusts (Figure 2A–D) consist of a fine-grained, homogeneous matrix of iron oxyhydroxides and silica containing dispersed volcanic particles and fragments of variable size and morphology. At higher magnification, some crust surfaces display ooidal textures characterized by well-developed concentric layering (Figure 2E), while others exhibit a ferruginous mat composed of dense filamentous structures (Figure 2F). Secondary euhedral gypsum crystals occur on ooidal crust surfaces (Figure 2G–H), forming prismatic to bladed habits on the iron oxyhydroxide substrate. Core sample CR1 shows distinct textural variations with depth. The uppermost interval is characterized by a silica-rich matrix with authigenic quartz crystals displaying well-developed prismatic forms (Figure 2M–N). Immediately below, the upper portion contains aggregates of marcasite crystals with complex intergrown habits (Figure 2I–J). An intermediate muddy interval deeper in the core contains a fine silica matrix with scattered euhedral gypsum and halite crystals (Figure 2K–L). Iron oxyhydroxide-dominated samples also exhibit skeletal crystal morphologies with irregular, branching outlines (Figure 2O–P). Euhedral to subhedral barite crystals with characteristic tabular to bladed habits occur as discrete phases within the sediment matrix (Figure 2Q–R). Samples of chimney-like structures display filamentous networks and tubular microstructures closely associated with iron oxyhydroxide precipitates (Figure 2S–T), forming complex three-dimensional frameworks distinct from the abiotic textures observed in the crust and core samples.

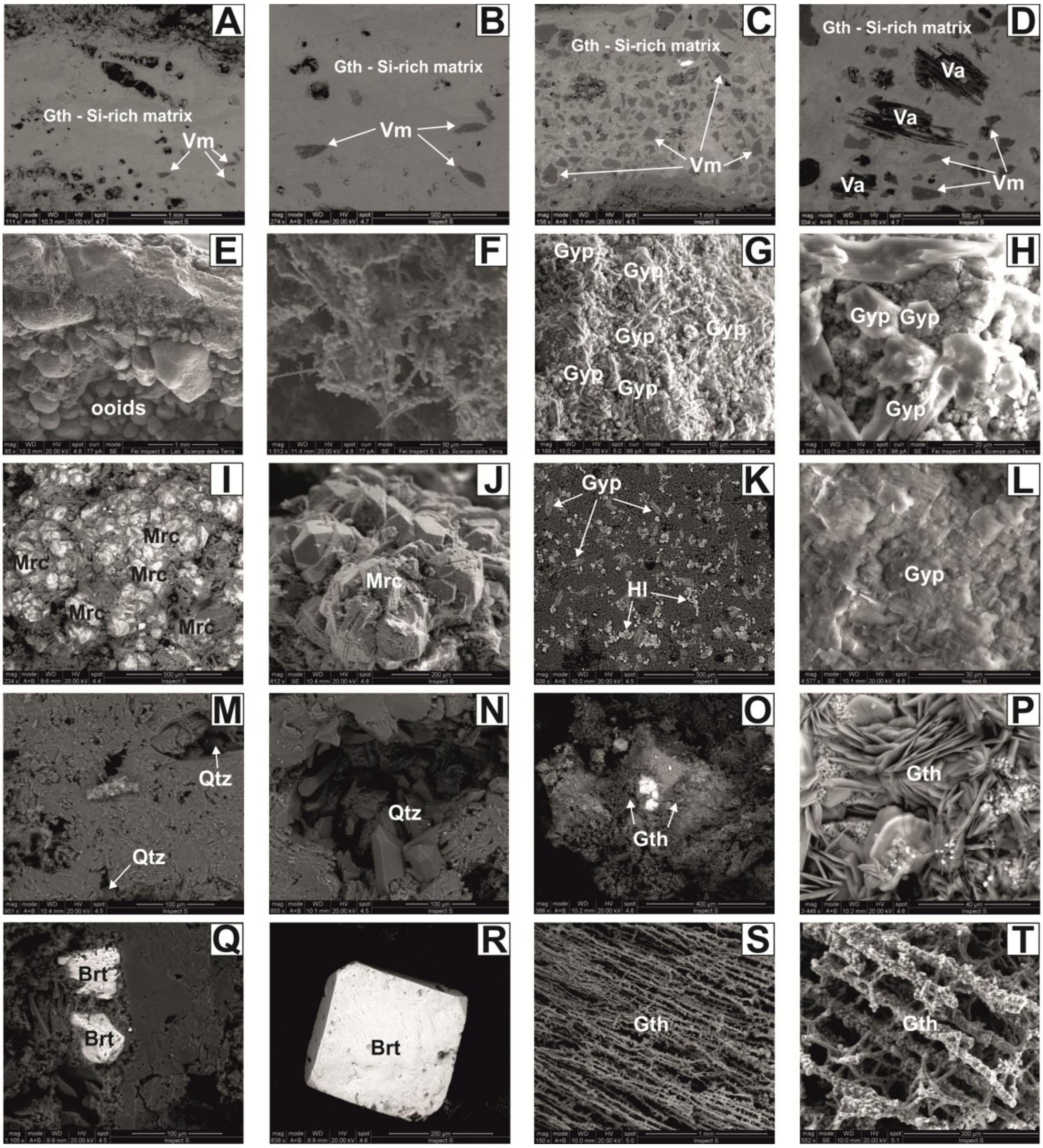

Figure 2. SEM images of hydrothermal sediments from Panarea Island. (**A**–**D**) BSE images of iron-rich crusts with goethite–silica matrix and dispersed volcanic mineral fragments; (**E**) ooids with concentric layering; (**F**) filamentous ferruginous mat suggestive of microbial iron precipitation; (**G**,**H**) euhedral gypsum crystals on ooidal crust surface, detail in (**H**); (**I**–**J**) marcasite crystal aggregates from upper core CR1, detail in (**J**); (**K**–**L**) authigenic gypsum and halite in microcrystalline silica matrix, intermediate interval of CR1, detail in (**L**); (**M**,**N**) authigenic quartz in silica-rich matrix, uppermost CR1, detail in (**N**); (**O**,**P**) skeletal goethite morphologies indicative of rapid precipitation, detail in (**P**); (**Q**,**R**) tabular to bladed barite crystals; (**S**,**T**) filamentous biogenic microstructures associated with goethite precipitates, "PAN1" (**S**) and "PAN2" (**T**) chimneys. Gth–goethite; Va– volcanic ash; Vm–volcanic minerals; Gyp–gypsum; Hl–halite; Qtz–quartz; Mrc–marcasite; Brt–barite.

3.2. Mineralogical Assemblage

X-ray diffraction with semi-quantitative Rietveld analysis identifies the principal mineral phases in hydrothermal sediments (Table S2 and Figure S2 for representative XRD patterns). Quantitative analysis of smectite is challenging because turbostratic disorder causes diffuse scattering that overlaps with contributions from amorphous components such as volcanic glass, opaline silica, and Fe-oxyhydroxides (see footnote †, Table S2). Therefore, the smectite abundances in Table S2 represent combined clay-amorphous phase estimates and should be interpreted as semi-quantitative.

X-ray diffraction patterns from ferruginous samples BN1, BN10, BN15, BAS1, BCP04, and chimney-like structures PAN1 and PAN2 (representative pattern shown in Figure S2) exhibit sharp, well-defined reflections characteristic of goethite (α-FeOOH), confirming it as the predominant iron-bearing mineral in these samples. Characteristic reflections at d-spacings of 4.18 Å (110), 2.69 Å (130), 2.45 Å (021), and 1.72 Å (221) match the orthorhombic goethite structure. Rietveld refinement using the fundamental parameters approach (BGMN) [46], where sample-related size broadening is modeled as a Lorentzian integral breadth (B1) and coherent domain size D = 1/B1 [47], yielded a mean isotropic coherent domain size of 8.1 ± 0.7 nm, with the uncertainty representing estimated standard deviation (e.s.d.) from the least-squares refinement. This value is representative of all ferruginous samples analyzed (n = 5), which yielded consistent crystallite sizes within analytical uncertainty. An anisotropic refinement (B1 = ANISO) performed on a representative sample yielded 9.1 ± 2.3 nm, 8.1 ± 1.2 nm, and 10.0 ± 3.3 nm perpendicular to the (110), (101), and (020) crystallographic planes, respectively; the differences are not statistically significant given the overlapping uncertainties, confirming a nearly equidimensional crystal morphology.

Among the feldspar-dominated samples, sanidine is the major phase in BN23, accompanied by goethite, cristobalite, and carbonate minerals (Mg-calcite and calcite). Albite dominates BN14, with significant anorthite, goethite, and minor quartz and halite, while BN21 contains roughly equal proportions of albite and sanidine, with quartz as a notable additional phase. BN16 is characterized by a simple two-phase assemblage of cristobalite and siderite, and BN18 is dominated by illite, along with albite and multiple silica polymorphs. Sample BCP07 is strongly dominated by kaolinite, with a rare svanbergite–woodhouseite APS mineral as an accessory phase (Figure 3).

Core samples CR1, CR1_liv0-3, and CR3 are all smectite-rich, each associated with feldspars and silica polymorphs in varying proportions. CR4 is dominated by disordered kaolinite, with a poorly crystalline component (~20 wt %) and minor jarosite and siderite. Sulphate minerals (gypsum, barite, jarosite), iron sulfides (marcasite), and carbonates (calcite, Mg-calcite, siderite) occur as accessory phases across several samples.

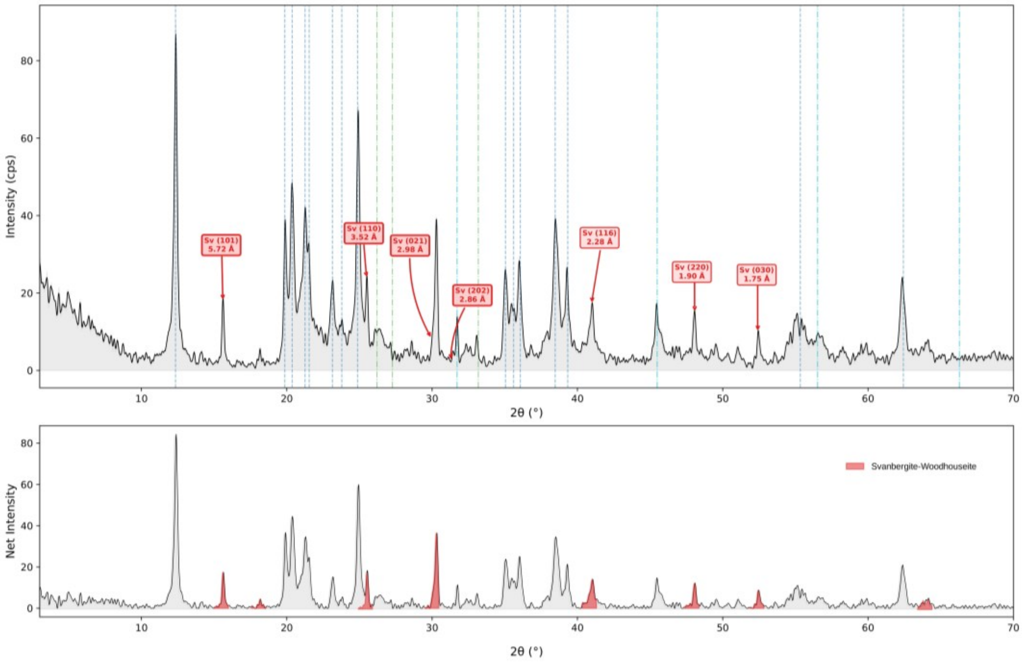

Figure 3. X-ray powder diffraction pattern of sample BCP07 (Cu Kα radiation, λ = 1.5418 Å). Upper panel: smoothed diffractogram with phase identification. Svanbergite–woodhouseite solid solution peaks are indicated by red-labeled boxes with Miller indices and d-spacings; kaolinite (blue dashed lines), halite (cyan dash-dot lines), and aragonite (green dash-dot lines) are also shown. The refined unit cell parameters (a = 6.975 Å, c = 16.584 Å) are consistent with an intermediate composition $(Sr_{0.78}Ca_{0.22})Al_3(PO_4)(SO_4)(OH)_6$ estimated by Vegard's law interpolation. Lower panel: background-subtracted net intensity with phase attribution (red = svanbergite–woodhouseite).

3.3. Major Element Geochemistry and Sample Classification

The analyzed hydrothermal sediments from Panarea Island reveal distinct geochemical groups based on major oxide compositions (Tables 2–4). Ferruginous, silica-dominated chimney fragments and core samples each display characteristic SiO_2-Fe_2O_3 relationships and other key oxide signatures that highlight their formation processes.

Ferruginous samples (BN1, BN10, BN15, BAS1, BCP04, PAN1, PAN2) are characterized by extremely high Fe_2O_3 (>77 wt %) and low SiO_2 (4–14 wt %). BN10 records the highest Fe_2O_3 (88 wt %) with minimal SiO_2 (4 wt %), while chimney-like samples PAN1 and PAN2 maintain similarly elevated Fe_2O_3 (~85–86 wt %) with slightly higher SiO_2 (~8–9 wt %). Al_2O_3 remains consistently low across this group (<4 wt %), and SO_3 is modest (<1.2 wt %).

Silica-dominated samples (BN14, BN16, BN18, BN20, BN21, BN23, BCP07) show high SiO_2 (48–72 wt %) inversely related to lower Fe_2O_3 (3–25 wt %). BN20 and BN21 have the highest SiO_2 (~70–72 wt %) with minimal Fe_2O_3. Al_2O_3 varies widely across the group (9–26 wt %), reaching its maximum in BCP07, where SO_3 also peaks at 4.5 wt %. Alkali contents are variable (Na_2O up to 8.4 wt % in BN16; K_2O up to 5.7 wt % in BN20), and CaO reaches 9 wt % in BN23.

Core samples display SiO_2 ranging from 53 to 83 wt % and uniformly low Fe_2O_3 (2–6 wt %). Near-surface intervals of CR1 show the highest SiO_2 contents (>80 wt %), which decrease downcore as Al_2O_3 rises, peaking at ~25 wt %. SO_3 decreases markedly with depth, from ~10 wt % near the surface to <0.4 wt % in CR3. CR3 records the highest alkali contents of the core samples (Na_2O 5.5 wt %, K_2O 4.0 wt %), while CR4 is distinguished by elevated Al_2O_3 (~22 wt %) and the highest Fe_2O_3 within the core group.

3.4. Trace Element Signatures

Ferruginous samples are characterized by exceptionally high concentrations of arsenic (As) and vanadium (V) (Table 2), reaching up to 844 ppm for As and 1030 ppm for V, which are among the most distinctive geochemical signatures of this facies. On the spider diagrams (Figure 4), these samples display negative barium (Ba) anomalies with consistently low values (22–96 ppm; BN1, BN15, BAS1, BCP04, PAN1, PAN2), although BN10 is an exception with an anomalously elevated Ba concentration of 1066 ppm. Zirconium (Zr) is variable (0–154 ppm; peaking at 154 ppm in BN10). Zinc (Zn) ranges moderately from 41–160 ppm, with peaks in BAS1 (160 ppm) and BN15 (159 ppm), whereas nickel (Ni) reaches up to 70 ppm in BN1. The PAN1 and PAN2 chimney-like structures subgroup deviates, showing low As anomalies, prominent positive molybdenum (Mo) spikes (171–199 ppm), negligible Zr (near 0 ppm), and lower Zn (41–48 ppm).

Silica-dominated samples show distinct positive anomalies for Ba, Zr, and Sr on spider diagrams, clearly distinguishing them from ferruginous samples. Ba displays pronounced enrichment, reaching up to 980 ppm in BCP07 and 965 ppm in BN18, accompanied by consistently elevated Zr (109–234 ppm, with a maximum of 234 ppm in BCP07). Strontium (Sr) shows similarly high values, up to 1320 ppm in BCP07. Lead (Pb) is enriched up to 289 ppm in BCP07, and As varies widely from 25 to 305 ppm, with the highest value in BN23 (305 ppm). Other elements, such as Zn (50–179 ppm; maximum in BN18), copper (Cu, 23–54 ppm), and molybdenum (Mo, 8–59 ppm), are present at moderate levels.

Core samples reveal complex, depth-stratified patterns on spider diagrams, with massive positive Ba anomalies in shallow intervals such as CR1 0–3 cm (46,976 ppm) and Zn spikes in deeper layers, including CR1 24–27 cm (1265 ppm) and CR4 (1920 ppm). These correspond with systematic Pb enrichment (81–407 ppm; maximum in CR1 24–27 cm), elevated Sr (434–2114 ppm; peaking in CR1 0–3 cm and 21–24 cm), and variable As (36–251 ppm). Vanadium (V) reaches 257 ppm in CR4, copper (Cu) up to 79 ppm, and molybdenum (Mo) up to 42 ppm, while Zr remains consistently moderate (137–379 ppm).

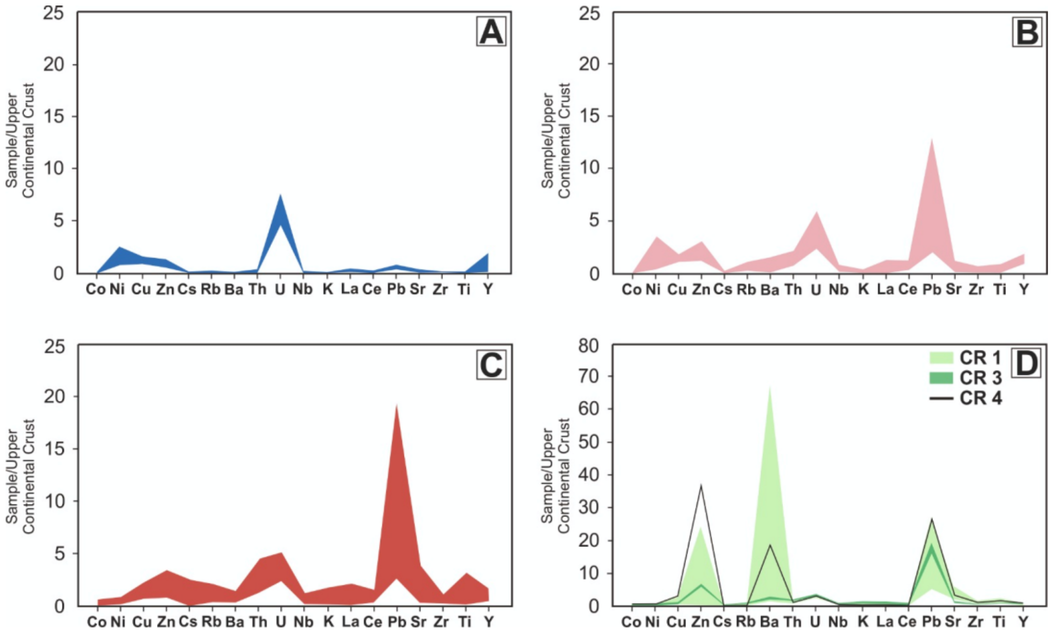

Figure 4. Trace element spider diagrams for the analyzed samples from Panarea Island, grouped as (**A**) chimney fragments; (**B**) ferruginous; (**C**) silica-dominated; and (**D**) core samples. Data have been normalized to the upper continental crust [48].

4. Discussion

4.1. Hydrothermal Facies: Textural and Mineralogical Constraints

The integrated textural (Figure 2) and mineralogical (Table S2) dataset from the Panarea hydrothermal sediments defines four hydrothermal facies, framed within the established classification scheme of hydrothermal alteration facies [49–51], which positions alteration assemblages according to their controlling temperature and pH conditions.

Low-temperature hydrothermal iron oxide facies (direct precipitate): The iron oxide facies is dominated by nanocrystalline goethite (α-FeOOH) forming crusts and chimney-like structures with three distinct textural types: (i) ferruginous mats of filamentous and tubular microstructures (PAN1, PAN2); (ii) well-developed ooidal textures with concentric layering (BAS1, BCP04); and (iii) dispersed volcanic glass shards and volcanic mineral crystals. This facies does not correspond to a hydrothermal alteration facies sensu stricto. Several lines of evidence support direct low-temperature oxidative precipitation at the fluid–seawater interface rather than fluid–rock interaction: (i) the mineralogical assemblage is dominated by a single nanocrystalline phase (goethite) with no secondary silicate or phyllosilicate alteration products that would be expected from fluid–rock interaction; (ii) the nearly equidimensional coherent domain size (8.1 ± 0.7 nm) is consistent with rapid precipitation from supersaturated fluids rather than dissolution-replacement reactions; (iii) the ooidal textures and filamentous microstructures are characteristic of Fe-oxyhydroxide accretion at a fluid–seawater mixing interface [34]; and (iv) the low venting temperature (<150 °C) at Basiluzzo [31] precludes the thermal conditions required for silicate mineral breakdown and secondary mineral formation. Quantitative Rietveld analysis reveals a mean isotropic coherent domain size of 8.1 ± 0.7 nm ($n = 5$), with anisotropic refinement confirming nearly equidimensional crystal morphology. This contrasts with the strongly acicular habit (axial ratios 2–5) of goethite crystallized at equilibrium from dilute solutions [51] and is consistent with rapid precipitation from highly supersaturated fluids suppressing preferential b-axis growth. The prominent filamentous networks in the most surficial ferruginous sediments are morphologically consistent with iron-oxidizing bacteria [51,52,53]; however, morphology alone does not constitute conclusive evidence of biogenicity, though microbial presence in analogous Panarea structures was previously confirmed by Bortoluzzi et al. [37].

Argillaceous to propylitic alteration facies (silica-clay assemblage): The silica-clay alteration facies is characterized by varying proportions of smectite-group clays, high-temperature silica polymorphs (cristobalite and tridymite), and feldspars (albite and sanidine). Core samples also contain plagioclase, phillipsite, barite, and maghemite. Maghemite is interpreted as a product of low-temperature oxidative transformation of primary volcanic magnetite, commonly documented in submarine hydrothermal environments where oxygenated seawater interacts with mafic volcanic substrates [54]. Phillipsite records the low-temperature, near-neutral pH end of the alteration spectrum (60–100 °C) [55], whereas diaspore (α-AlOOH) reflects episodic highly acidic and aluminous conditions at elevated temperatures, consistent with advanced argillic alteration [56]. Textures include a microcrystalline silica groundmass with dispersed clays, well-faceted authigenic quartz, and pseudomorphic replacement of volcanic glass. Smectite-bearing assemblages are consistent with argillaceous alteration facies (pH~5.5–7, T < 160 °C) [50,56,57,58]. The co-occurrence of sanidine (> 200 °C) and high-temperature silica polymorphs in samples CR3 and BN23 aligns more closely with propylitic alteration conditions (pH 5.5–7, T = 230–350 °C) [17,59]. Cristobalite and tridymite should be interpreted cautiously, as both may also originate from low-temperature devitrification of volcanic glass [58,60]. Sanidine provides stronger evidence for elevated temperatures, since its formation requires structural reorganization not achievable by devitrification alone. The coexistence of high- and low-temperature phases reflects fluid mixing, temporal cooling, or inheritance of primary volcanic mineralogy rather than a contradiction. The inferred temperature range of 200–350 °C for peripheral zones should be considered a qualitative estimate broadly consistent with Italiano and Nuccio [31], as no direct fluid temperature measurements were performed. Carbonate minerals (Mg-calcite, calcite) detected in dredged sediments such as BN23 are interpreted as biogenic debris from the shallow marine environment (81 m depth), consistent with their occurrence exclusively in dredged surface sediments and their morphological characteristics (fragmented shell debris observed in the collected sample; Figure S1I), rather than as hydrothermal precipitates.

Phyllic to propylitic alteration facies (sulfate-sulfide assemblage): The sulfate and sulfide assemblages represent the oxidized and reduced ends of a redox-stratified continuum, broadly consistent with phyllic to propylitic alteration facies conditions (pH 5.5–7, T = 160–350 °C) [61–63]. The sulfate component, including barite and gypsum as euhedral crystals in shallow core intervals and disseminated grains in muddy sediments, records exceptional Ba enrichment (up to 46,976 ppm) from mixing Ba-rich hydrothermal fluids with sulfate-bearing seawater at the sediment–water interface, with concentrations decreasing with depth [63–66]. Halite and gypsum are physically enclosed within consolidated silica clasts, confirming their authigenic origin and ruling out surface crystallization from residual seawater (removed by distilled water washing prior to drying; Section 2). Their co-occurrence is consistent with crystallization from Cl^--enriched hydrothermal pore fluids concentrated within sediment porosity during diagenesis. The sulfide component consists of marcasite and pyrite as framboidal aggregates, euhedral crystals, and disseminated grains in anoxic subsurface sediments, where bacterial sulfate reduction drives iron sulfide precipitation; marcasite specifically indicates localized acidic conditions [67,68]. Both components accumulate base metals (Zn, Pb, Cu) through sulfide precipitation and metal adsorption. Their depth-controlled coexistence, with some samples containing both oxidized and reduced phases, reflects the gradient between oxidizing near-surface and reducing subsurface conditions and temporal redox variations [17,34,59].

Advanced argillic alteration facies (acid-sulfate assemblage): The acid-sulfate alteration facies, equivalent to the advanced argillic alteration facies (pH 2–4, T = 160–300 °C) [49,50], is characterized at Panarea by nearly monomineralic kaolinite, with svanbergite, jarosite, cristobalite, and, in some samples, disordered kaolinite, amorphous components, quartz, pyrite, and siderite. Textures include cryptocrystalline kaolinite aggregates, advanced mineral replacement, and vuggy porosity. Kaolinite forms through advanced hydrolysis of silicate phases under high H^+ activity (pH~4–6, T < 200 °C) [66], while associated APS minerals and jarosite confirm highly acidic conditions from sulfide oxidation or magmatic SO_2 degassing [66,67]. The stability fields of these phases further constrain alteration conditions: jarosite is stable at T < 90 °C (pH 1.5–3) [68], consistent with near-surface sulfide oxidation, while svanbergite–woodhouseite forms at T = 100–250 °C [66,69], indicating deeper or earlier-stage alteration. APS minerals in kaolinite-bearing deposits can be more sensitive to physicochemical indicators than phyllosilicates alone [66]. The intermediate svanbergite–woodhouseite composition ($Sr_{0.78}Ca_{0.22}$) in BCP07 reflects the Sr/Ca ratio of the precipitating fluid: the dominance of the Sr-rich endmember indicates interaction with Sr-bearing volcanic plagioclase of the Aeolian arc, while the 22 mol % Ca component is consistent with the Ca-enriched Panarea thermal waters [31]. This composition was estimated from Vegard's law using the Rietveld-refined unit cell parameter and should be considered a bulk average, as crystal-scale variations cannot be assessed at this stage. Rietveld refinement combined with the high bulk Sr content (1320 ppm in BCP07; Table 2) provides consistent evidence for the presence of svanbergite, representing the first documented occurrence of an APS mineral at Panarea. Future investigations employing complementary analytical techniques would allow crystal-scale compositional characterization and further consolidate this identification. The coexistence of pyrite with kaolinite and jarosite indicates localized redox variations, and the spatial restriction of this facies to discrete zones of magmatic volatile input reflects pronounced pH gradients in laterally zoned alteration systems [70].

The spatial distribution of the four facies reflects systematic zonation controlled by temperature, pH, redox conditions, and degree of seawater interaction, summarized in the temperature-pH stability diagram (Figure 5). The low-temperature iron oxide precipitate dominates the fluid–seawater mixing zone around Basiluzzo (<150 °C). Argillaceous to propylitic alteration assemblages characterize peripheral zones at circumneutral pH. Advanced argillaceous (acid-sulfate) alteration is restricted to discrete zones of intense magmatic volatile input, and the redox-stratified sulfate-sulfide continuum records depth-controlled fluid evolution from oxidizing near-surface to reducing subsurface conditions [34]. This zonation is broadly consistent with the hydrothermal alteration zonation documented in active hydrothermal systems [49,50], adapted here to a shallow submarine volcanic setting where enhanced seawater interaction, high oxygen availability, and proximity to subaerial volcanic inputs modify the classic alteration patterns observed in continental geothermal fields.

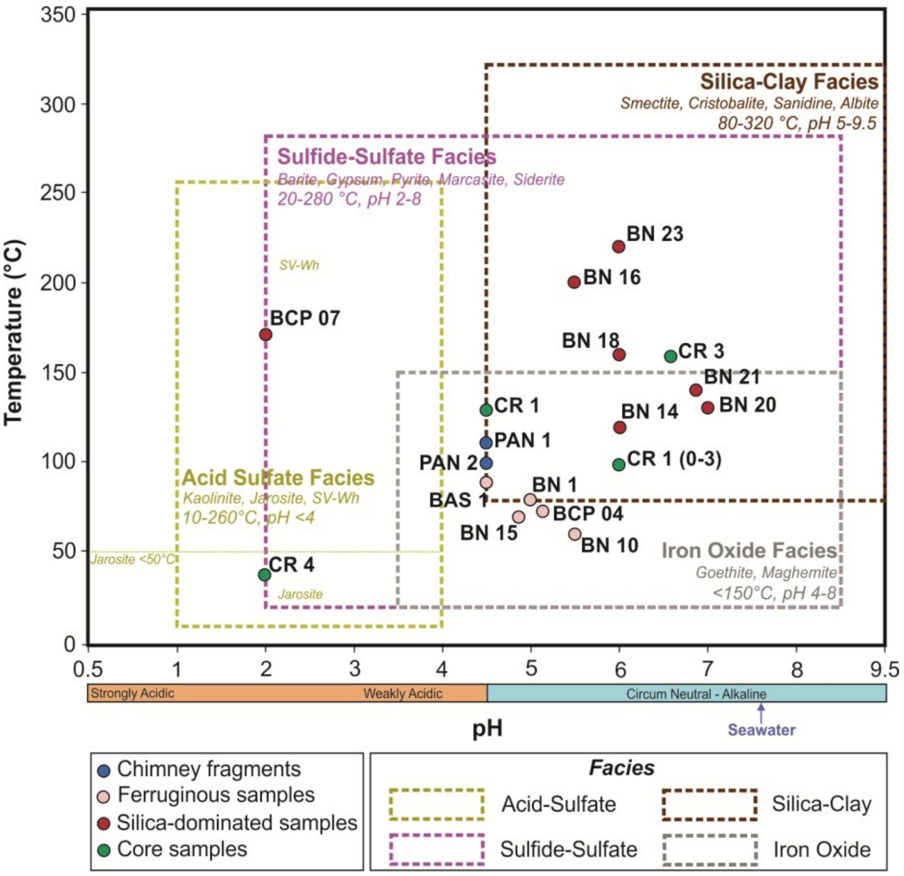

Figure 5. Temperature–pH diagram showing stability fields for the four hydrothermal facies identified at Panarea and the positions of analyzed samples. Stability fields are based on Rietveld quantitative mineralogy, bulk XRF geochemistry, and published thermodynamic data [51,58,66,68,69,71]. Sample positions are estimated from dominant hydrothermal mineral assemblages; non-hydrothermal phases (biogenic carbonates, detrital minerals) are excluded. No direct fluid temperature measurements were obtained; all temperature assignments are qualitative. Seawater pH (8.1) is shown for reference (dashed vertical line). Sv–Wh = svanbergite–woodhouseite solid solution. Symbol shapes: circle = dredge/surface sediment; square = chimney fragment; triangle = core sample. Symbol colors correspond to facies affiliation.

4.2. Geochemical Signatures and Metal Sequestration Processes

Major oxide and trace element compositions of Panarea hydrothermal sediments exhibit distinct geochemical signatures that reflect different mineralogical assemblages, variable fluid chemistry, and specific formation processes within this shallow submarine volcanic system. The integrated mineralogical, geochemical, and textural dataset reveals clear spatial zonation of hydrothermal activity corresponding to distinct temperature regimes and metal sequestration pathways (Figure 5).

Low-temperature Fe-oxyhydroxides form under oxidizing conditions where redox-sensitive elements are readily incorporated into rapidly precipitating Fe(III) structures [29,33,34]. Trace element incorporation into nanocrystalline goethite reflects element-specific crystal-chemical, surface-chemical, and redox controls. Vanadium incorporates via Fe(III) substitution in octahedral sites (V^{5+}/Fe^{3+} ionic radii similarity) and surface adsorption onto goethite hydroxyl groups at pH 4–8 [72], enhanced by the high surface area-to-volume ratio of the ~8 nm equidimensional crystallites. Arsenic is scavenged via surface complexation under oxidizing conditions [73], consistent with concentrations up to 844 ppm. Molybdenum enrichment (171–199 ppm in chimney structures) reflects Fe-oxyhydroxide surface adsorption under suboxic conditions [74], with possible biological mediation by iron-oxidizing bacteria [75]. Cobalt depletion reflects the absence of Mn-oxide phases required for oxidative $Co^{2+} \rightarrow Co^{3+}$ scavenging, precluded by low MnO contents (0.01–0.90 wt %) and dominance of Fe(III) oxyhydroxide precipitation [76,77]. Metalloid scavenging by Fe-oxyhydroxides is the dominant sequestration mechanism at Basiluzzo, with V among the highest reported for Mediterranean hydrothermal systems and As among the highest in the Tyrrhenian–Aeolian domain, comparable to western Pacific anlogs where As mobilization and co-precipitation with iron oxides are dominant [78,79], establishing Panarea's ferruginous facies as a metalloid endmember in the Mediterranean domain (Section 4.3). Conversely, systematic Ba depletion (14–96 ppm) and low Zr (0–154 ppm), evident as negative spider diagram anomalies, distinguish these precipitates from detrital or volcanic inputs. Ba depletion reflects minimal barite precipitation and low goethite incorporation, while low Zr indicates negligible aluminosilicate contamination.

The chimney-like structures subgroup (PAN1, PAN2) displays a distinctive signature with subdued As anomalies, prominent Mo spikes (171–199 ppm), and near-zero Zr. Elevated Mo is primarily attributed to abiotic adsorption onto Fe-oxyhydroxides under fluctuating redox conditions, a well-characterized process that selectively enriches Mo relative to As during oscillating oxidation-reduction cycles [74,80,81]. Incorporation into reduced sulfide phases under slightly more reducing conditions represents an additional contributing mechanism. The prominent filamentous networks observed in the textures of these samples are consistent with microbial iron oxidation, suggesting that biological uptake or complexation with extracellular polymeric substances [79] may represent a subsequent control on Mo sequestration, potentially overprinting or further enhancing the initial abiotic enrichment. Mo isotope data, EPS characterization, and direct microbial evidence are needed to fully constrain the timing and relative contributions of biotic and abiotic pathways [75].

Silica-dominated samples (BN14, BN16, BN18, BN20, BN21, BN23, BCP07) define a compositional trend toward high SiO_2 (48–72 wt %) with correspondingly lower Fe_2O_3 (2.6–25 wt %), reflecting intense silicification or incorporation of volcanic glass and high-temperature silica polymorphs. Elevated Al_2O_3 (up to 25 wt % in BCP07) correlates with clay minerals (kaolinite, smectite) and feldspars, indicating variable degrees of hydrothermal alteration of volcanic precursors. The wide range in alkali contents (Na_2O up to 8.37 wt %; K_2O up to 5.71 wt %) reflects the preservation of primary volcanic feldspars (albite and sanidine) in some samples versus their alteration to clays in others. Sample BCP07, with the highest SO_3 (4.49 wt %), corresponds to the kaolinite–svanbergite assemblage discussed above, confirming acid-sulfate alteration in higher-temperature zones. Spider diagrams for silica-dominated samples show distinct positive Ba and Zr anomalies, clearly distinguishing them from ferruginous samples. Ba enrichment is pronounced (up to 980 ppm in BCP07), accompanied by elevated Sr (up to 1320 ppm), reflecting the presence of barite and/or incorporation into altered feldspars and clays. High Zr concentrations (109–234 ppm) indicate retention of accessory zircon or incorporation of volcanic glass shards, consistent with textural observations of lithic fragments within the Fe–Si matrix. Variable As enrichment (25–305 ppm) suggests localized iron oxide precipitation superimposed on the siliceous-aluminosilicate matrix.

Core samples reveal systematic depth-controlled variations in major oxides and trace elements reflecting evolving redox conditions and fluid–sediment interactions. Near-surface intervals show maximum SiO_2 (up to 82.59 wt %) with depleted Fe_2O_3 (<2 wt %), consistent with silica-rich hydrothermal precipitates or amorphous silica. With increasing depth, SiO_2 decreases while Al_2O_3 increases (up to 25.33 wt %), marking a transition to clay-dominated assemblages (smectite, kaolinite). Strong SO_3 depletion with depth, from 10.03 wt % at 0–3 cm to 0.38 wt % at deeper intervals, reflects progressive loss of sulfate minerals and bacterial sulfate reduction in anoxic subsurface zones, consistent with the occurrence of framboidal pyrite and marcasite. Spider diagrams reveal complex depth-stratified patterns: shallow intervals display massive positive Ba anomalies (up to 46,976 ppm in CR1 0–3 cm), documenting exceptional barite enrichment from the mixing of Ba-rich hydrothermal fluids with sulfate-bearing seawater at the sediment–water interface, indicative of strong fluid discharge at steep chemical gradients [62,63]. Deeper intervals display pronounced Zn spikes (up to 1920 ppm in CR4) with elevated Pb (up to 407 ppm), Cu (up to 79 ppm), and V (up to 257 ppm), reflecting sulfide mineral accumulation under reducing conditions. The transition from sulfate-dominated upper to Zn-enriched deeper layers records temporal shifts in hydrothermal flux and redox conditions, and these vertical gradients may provide stratigraphic archives suitable for future high-resolution geochronological studies.

The integrated dataset supports a genetic model of fault-controlled seawater circulation along distinct thermal pathways, with important implications for trace metal cycling in shallow marine volcanic environments. Low-temperature pathways around Basiluzzo (~100–150 °C) leach Fe, Mn, As, V, and Mo from volcanic substrates, with magmatic CO_2 input enhancing metal solubility. Upon seafloor discharge, rapid abiotic and biologically mediated Fe(II) oxidation produces nanocrystalline goethite precipitates that effectively scavenge metalloids and prevent their dispersal into the water column. Higher-temperature pathways reach 200–350 °C at greater crustal depths, driving extensive silicate alteration and generating fluids enriched in Si, Ba, Sr, and alkali elements. The coexistence of oxidized and reduced mineral assemblages indicates dynamic redox fluctuations controlled by variations in fluid flux, bacterial sulfate reduction, and episodic oxidative weathering of primary sulfides. The high concentrations of As, V, Mo, Pb, and Zn across sample types indicate that shallow hydrothermal systems can act as significant point sources for trace metal input to coastal marine environments, with important biogeochemical and ecological consequences warranting further investigation.

4.3. Classification and Comparative Framework: Mediterranean and Global Hydrothermal Systems

Among the four facies identified at Panarea, the ferruginous facies is particularly distinctive in the Mediterranean context. Fe-oxyhydroxide deposits from other Aeolian–Tyrrhenian hydrothermal systems show substantially lower metalloid concentrations, As~20–150 ppm and V~30–280 ppm in Fe-rich crusts across the arc [14] and As typically below 200 ppm in hydrothermal sediments from the same province [15]. These values are exceeded at Panarea, where As reaches up to 844 ppm (BN1) and V up to 1030 ppm

(BAS1), establishing the Basiluzzo low-temperature system as a metalloid endmember in the Mediterranean domain.

In the (Co + Ni + Cu) × 10-Fe-Mn ternary diagram (Figure 6A), ferruginous samples plot within the hydrothermal iron oxide field, consistent with goethite-dominated low-temperature oxidative precipitation, while silica-dominated and core samples extend toward mixed hydrothermal-volcaniclastic compositions. The Co/Zn vs. Co + Ni + Cu plot (Figure 6B) confirms the hydrothermal origin of all Panarea samples, which occupy a hydrogenous/hydrothermal transitional field typical of low- to intermediate-temperature systems, distinct from high-temperature mid-ocean ridge black smokers. The Zn-(Ni + Co)-(As + Mo) diagram (Figure 6C) places Panarea between the East Pacific Rise and Western Woodlark Basin fields; elevated As + Mo distinguishes it from basalt-hosted EPR systems, indicating greater sediment interaction and more oxidizing conditions. In the Cu-Pb × 10-Zn diagram (Figure 6D), core samples plot toward the Zn-Pb apex, resembling Kuroko-type and back-arc basin deposits (Okinawa, Lau, and Fiji), consistent with subsurface sulfide precipitation and metal remobilization [82]. Immobile element ratios (Nb/Ti, Zr/Nb, and La/Y; Figure 6E,F) confirm that many samples retain volcanic protolith signatures consistent with calc-alkaline to shoshonitic magmas of the Aeolian arc [26–28].

The overall compositional range, from iron-rich precipitates to silica-aluminosilicate assemblages to base metal-enriched sulfidic sediments, is comparable to back-arc basin hydrothermal systems [83], though the shallow setting (37–207 m) imparts distinctive features: enhanced oxygen availability promotes extensive goethite precipitation, greater seawater mixing facilitates barite formation, and proximity to subaerial volcanic inputs contributes high-temperature silica polymorphs. Comparison with the Savelli et al. [13] compositional field (gray field in Figure 6) confirms general agreement for ferruginous and silica-dominated surface samples, validating the present dataset and the long-lived nature of iron oxide and silica precipitation at Panarea. However, the exceptional Ba concentrations in core samples (up to 46,976 ppm in CR1 0–3 cm) and elevated Zn-Pb concentrations fall outside the Savelli et al. [13] field, which was based exclusively on surface precipitates. This discrepancy reflects a genuine difference in sampling strategy rather than contradiction: subsurface barite enrichment and depth-controlled sulfide accumulation represent newly recognized geochemical endmembers for the Panarea system, documenting vigorous subsurface Ba flux and active biogeochemical cycling not captured in earlier surface-focused studies.

Panarea occupies a distinctive intermediate position within the Mediterranean hydrothermal domain. At Milos (Greece; 5–20 m depth), As in Fe-oxyhydroxide precipitates reaches up to 1200 ppm, exceeding the 844 ppm maximum at Panarea, due to more acidic fluids (pH 2–6 vs. pH 3–7.5) that substantially enhance As mobility [84,85]. However, V at Milos is typically only 30–120 ppm, and Mo is not anomalous, in stark contrast to the exceptional V (up to 1030 ppm) and Mo enrichment (171–199 ppm in chimneys) at Panarea. Milos sediments also show lower base metal (Zn, Pb, and Cu) concentrations, suggesting less water–rock interaction or different fluid source characteristics. At Vulcano (Italy; 0–20 m depth), shallow submarine fumarolic activity produces Fe-oxyhydroxide-rich sediments enriched in As (50–300 ppm), Sb, and Hg, but with lower V (80–200 ppm) and base metal concentrations, reflecting a more gas-dominated regime with less water–rock interaction than at Panarea [84,86]. Panarea's fluid pH (3–7.5) is less acidic than Milos, limiting As mobilization relative to that system, but more acidic than seawater-dominated ridge systems, enabling significant As and V scavenging by goethite, while greater water–rock interaction than at Vulcano accounts for elevated Zn, Pb, and Ba. The combined As–V–Mo–Ba–Zn signature of Panarea, reflecting a specific combination of fluid temperature, pH, redox conditions, and biological mediation, is unique within the Aeolian arc and unreplicated at either Milos or Vulcano.

https://doi.org/10.3390/min16050505

Beyond the Mediterranean, Panarea compares favorably with shallow arc hydrothermal systems worldwide. The Ambitle Island system (Papua New Guinea; 5–30 m depth, 50–98 °C) also produces Fe(III) oxyhydroxide deposits with extreme Fe enrichment, elevated As, and evidence of microbial mediation, though more acidic fluids (pH 5.2–5.8) result in higher dissolved metal concentrations than at Panarea [86]. Western Pacific systems, including Kagoshima Bay (Japan) and White Island (New Zealand), share similar shallow-water arc-volcanic settings with significant As–Fe co-precipitation and biological involvement in mineral precipitation. Element ratio plots confirm compositional consistency with other Mediterranean shallow-water vents [14,15,84], though Panarea exhibits its unique characteristics attributable to its local geological setting. Panarea is nonetheless distinctive in hosting both low-temperature iron oxide zones and higher-temperature silicate alteration within a small geographic area (~2 km^2), representing an exceptional natural laboratory for studying hydrothermal spatial zonation and the interplay between abiotic geochemical processes and biological mediation in shallow submarine volcanic systems.

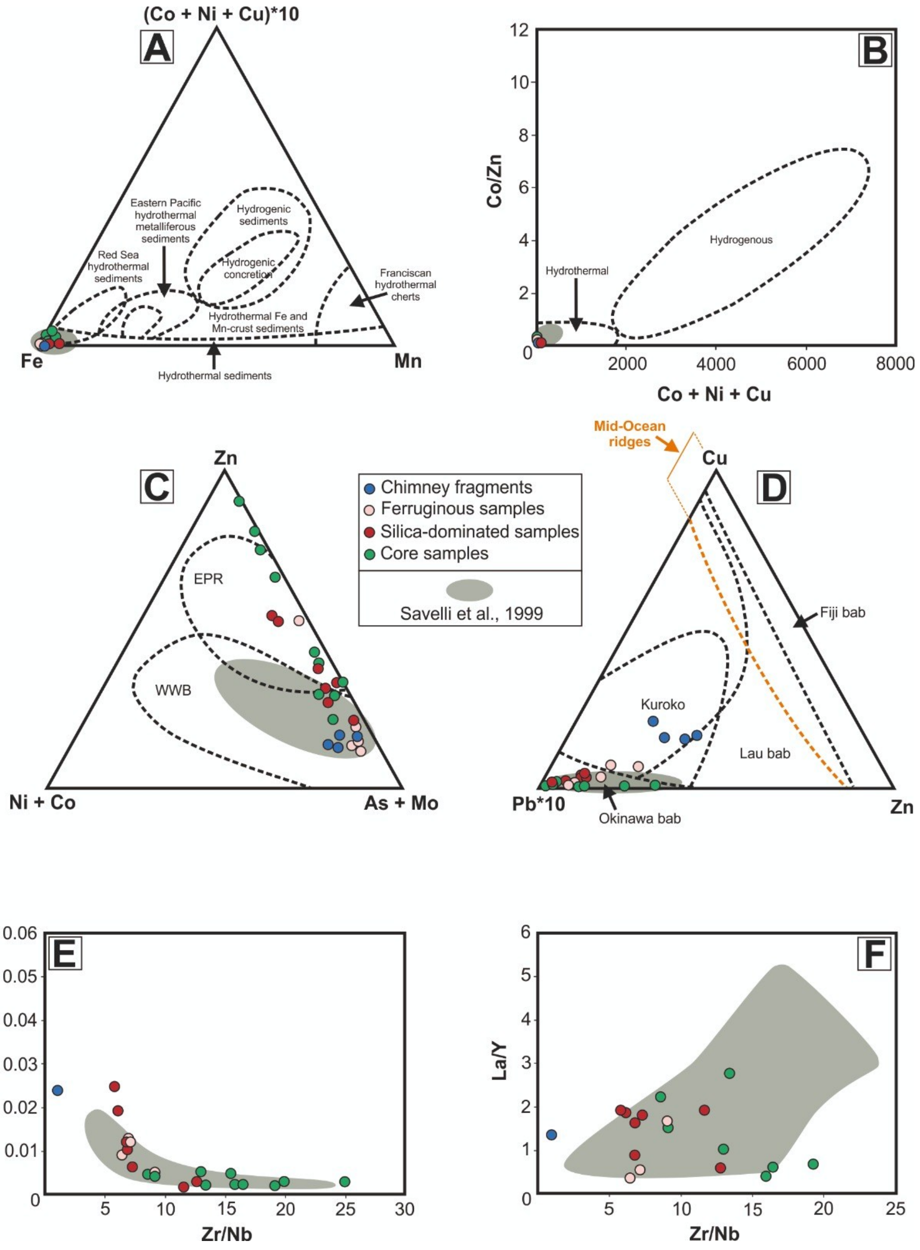

Figure 6. Geochemical discrimination and variation diagrams for classification of hydrothermal sediments from Panarea. (**A**) Ternary diagram of (Co + Ni + Cu) × 10–Fe–Mn showing compositional fields of different hydrothermal sediment types and hydrogenous deposits; (**B**) bivariate plot of Co/Zn vs. Co + Ni + Cu distinguishing hydrogenous from hydrothermal origins; (**C**) ternary diagram of Zn–(Ni + Co)–(As + Mo) showing East Pacific Rise (EPR) [87] and Western Woodlark Basin (WWB) [88] hydrothermal fields; (**D**) ternary diagram of Cu–Pb × 10–Zn displaying compositional trends for mid-ocean ridge and back-arc basin systems (Kuroko, Okinawa back-arc basin (bab), Lau bab, and Fiji bab); (**E**) Nb/Ti vs. Zr/Nb; (**F**) La/Y vs. Zr/Nb. Sample types: chimney fragments (blue), ferruginous samples (grey), silica-dominated samples (red), and core samples (green). Grey field represents compositional range from Savelli et al. [13].

4.4. Panarea as a Natural Laboratory to Study Metal Precipitation

The Panarea hydrothermal system serves as an accessible natural laboratory for studying the formation of seafloor Fe-rich deposits across various temperature regimes. Shallow water depths (37–207 m) and active hydrothermal discharge at multiple temperature settings allow for ROV and scuba-based observations and time-series monitoring that are otherwise logistically challenging in deep-sea systems. Although Fe_2O_3 concentrations in Basiluzzo deposits (77–88 wt %) rival those of terrestrial hematite ores, small deposit volumes, high water content, and protected status preclude extraction. Nonetheless, geochemical characterization provides baseline data relevant to ongoing discussions on seafloor mineral resource exploitation (e.g., [8,12]). Extreme enrichments in As, V, Mo, and Ba show that shallow hydrothermal systems can generate significant local metal concentrations, while insights into metal cycling and mineral-microbe interactions inform predictive models for ancient and modern seafloor mineralization in volcanic arc settings worldwide. The fault-controlled thermal architecture, with geothermal gradients of 150–350 °C at depth [34] and sustained magmatic CO_2 input, offers a structurally accessible analog for shallow low-enthalpy geothermal reservoirs within the Aeolian arc, which is increasingly relevant for renewable energy assessment [89,90]. The co-enrichment of EU-listed critical raw materials, especially V, Mo, and Zn, within distinct hydrothermal facies further underscores the scientific value of this system for understanding element mobility and sequestration in submarine volcanic environments.

5. Conclusions

This integrated study identifies four hydrothermal facies at Panarea, framed within the established hydrothermal alteration classification and reflecting temperature-dependent metal partitioning across the system. The low-temperature iron oxide direct precipitate, nanocrystalline goethite with nearly equidimensional coherent domains of 8.1 ± 0.7 nm, forms by direct oxidative precipitation at the fluid-seawater interface around Basiluzzo (<150 °C), rather than by fluid-rock interaction sensu stricto. It displays high Fe_2O_3 (77–88 wt %), extreme As (up to 844 ppm) and V (up to 1030 ppm), and a distinctive Mo-enriched (171–199 ppm), As-depleted chimney signature attributed to differential microbial mediation. This combined As–V–Mo fingerprint establishes Panarea as a metalloid endmember among Mediterranean shallow-water hydrothermal systems.

The *argillaceous to propylitic alteration facies* contains smectite-group clays consistent with argillaceous conditions (pH~5.5–7, T < 160 °C), with sanidine and high-temperature silica polymorphs (cristobalite, tridymite) in samples CR3 and BN23, suggesting propylitic conditions (T = 230–350 °C) in peripheral zones. Temperature estimates from mineralogical proxies should be regarded as qualitative indicators only. The *phyllic to propylitic alteration facies* records systematic vertical redox stratification, from sulfate-dominated near-surface intervals (Ba up to 46,976 ppm in CR1 0–3 cm) to base-metal sulfide accumulations at depth (Zn up to 1920 ppm in CR4), documenting evolving hydrothermal flux and bacterial sulfate reduction. The co-occurrence of elevated SO_3 (7.80 wt %), high Zn (1265 ppm), and Ba (19,091 ppm) in the same interval (CR1 24–27 cm) indicates that the redox transition is not a sharp boundary but rather a mixed redox zone where sulfate and sulfide phases transiently coexist; this is consistent with oscillation of the sulfate reduction front driven by episodic variations in hydrothermal fluid flux, rather than a simple static vertical gradient [91]. The *advanced argillaceous alteration facies* is characterized by kaolinite, jarosite, and the first documented APS mineral at Panarea, svanbergite–woodhouseite ($Sr_{0.78}Ca_{0.22}$), providing new constraints on fluid Sr/Ca ratios during acid-sulfate alteration.

Spatial zonation, broadly consistent with hydrothermal alteration zonation in active geothermal systems, shows clear separation between the low-temperature Basiluzzo area, dominated by metalloid scavenging, and peripheral higher-temperature zones of silicate alteration and sulfate mineral formation. This pattern is adapted here to a shallow submarine setting where enhanced seawater interaction and high oxygen availability modify classic alteration patterns. The integrated dataset supports a genetic model of fault-controlled seawater circulation with magmatic CO_2 input and episodic redox fluctuations. Extreme metalloid concentrations, among the highest in the Mediterranean domain and comparable to western Pacific arc systems, together with the co-enrichment of EU-listed critical raw materials (V, Mo, and Zn) within distinct facies, provide a mineralogical framework relevant to understanding CRM cycling in submarine volcanic systems. The documented thermal zonation also offers reference constraints for geothermal potential assessment in the Aeolian arc.

Supplementary Materials: The following supporting information can be downloaded at https://www.mdpi.com/article/10.3390/min16050505/s1, Table S1: Rietveld refinement quality-of-fit metrics and refined phase assemblages for Panarea hydrothermal sediment samples; Table S2: Semi-quantitative mineralogical compositions (wt %) of Panarea Island samples, determined by Rietveld refinement of XRD data. Ferruginous samples are excluded as they consist entirely of goethite. Figure S1: Photographs of hydrothermal sediments from the Panarea Island study area. Panels (A–R) show representative samples illustrating the diversity of precipitates, including iron-rich crusts, sulfur-bearing sediments, and mixed lithologies from the submarine hydrothermal system (research cruise "PANA15", R/V Astrea). Panels (L) and (M) depict external portions of chimney fragments PAN1 and PAN2. Panels (N–P) show sediment cores CR1, CR3, and CR4, respectively (research cruise "PANA13", R/V Magnaghi). Figure S2: XRPD patterns of the main classified groups of the samples studied. BN10 and BCP04 as representatives for the "Low-temperature iron oxide facies"; BN14 and BN23 as representatives for the "Argillic to propylitic facies"; CR1 for the "Phyllic to propylitic facies"; CR4 as representative of the "Advanced argillic facies".

Author Contributions: Conceptualization, M.D.B. and G.S.; methodology, M.D.B. and G.S.; software, M.D.B. and G.S.; validation, M.D.B. and G.S.; formal analysis, M.D.B., D.R. and G.S.; investigation, M.D.B. and G.S.; resources, M.D.B., F.I., T.R. and G.S.; data curation, M.D.B., D.R., G.D.R., G.S. and A.T.; writing—original draft preparation, M.D.B.; writing—review and editing, M.D.B., D.R., V.E., F.I., V.V. and G.S.; supervision, M.D.B.; funding, F.I.; project administration, M.D.B., F.I. and G.S. All authors have read and agreed to the published version of the manuscript.

Funding: The paper is a scientific contribution to the project "Marine Hazard–Development of innovative technologies for identification, monitoring, and mitigation of natural and anthropic contamination processes", PON03PE_00203_1, funded by MUR—Italian Ministry of University and Research - OR1 coordinated by one of the authors (F.I.).

Data Availability Statement: The original contributions presented in this study are included in the article/Supplementary Materials. Further inquiries can be directed to the corresponding author.

Acknowledgments: The authors would like to thank the anonymous reviewers and the editor for their constructive comments and suggestions, which greatly contributed to improving the quality of the manuscript. We are grateful to the crews of the research vessels that participated in the surveys during the 2013–2015 research cruises: "A. Magnaghi" of Istituto Idrografico Militare; R/V "Astrea" of ISPRA, N/O; and to the colleagues of ISPRA, who participated in the fieldwork. We also acknowledge the Panarea ECCSEL NatLab–Italy laboratory of OGS, a facility of ECCSEL–ERIC (The European Carbon Dioxide Capture and Storage Research Infrastructure), for providing the SEM analyses conducted for this research.

Conflicts of Interest: The authors declare no conflicts of interest.

References

1. Tivey, M.K. Generation of seafloor hydrothermal vent fluids and associated mineral deposits. *Oceanography* **2007**, *20*, 50–65. https://doi.org/10.5670/oceanog.2007.80.
2. Hannington, M.; Jamieson, J.; Monecke, T.; Petersen, S.; Beaulieu, S. The abundance of seafloor massive sulfide deposits. *Geology* **2011**, *39*, 1155–1158. https://doi.org/10.1130/G32468.1.
3. German, C.R.; Seyfried, W.E. Hydrothermal Processes. In *Treatise on Geochemistry*, 2nd ed.; Holland, H.D., Turekian, K.K., Eds.; Elsevier: Oxford, UK, 2014; Volume 8, pp. 191–233. https://doi.org/10.1016/B978-0-08-095975-7.00607-0.
4. Hannington, M.D.; Jonasson, I.R.; Herzig, P.M.; Petersen, S. Physical and chemical processes of seafloor mineralization. In *Physical, Chemical, Biological and Geological Interactions Within Hydrothermal Systems*; Humphris, S., Fornari, D., Zierenberg, R., Eds.; American Geophysical Union Monograph: Washington, DC, USA, 1995; Volume 91, pp. 115–157.
5. Fouquet, Y.; Cambon, P.; Etoubleau, J.; Charlou, J.L.; Ondreas, H.; Barriga, F.J.A.S.; Cherkashov, G.; Semkova, T.; Poroshina, I.; Bohn, M.; et al. Geodiversity of hydrothermal processes along the Mid-Atlantic Ridge and ultramafic-hosted mineralization: A new type of oceanic Cu-Zn-Co-Au volcanogenic massive sulfide deposit. In *Diversity of Hydrothermal Systems on Slow Spreading Ocean Ridges*; Rona, P.A., Devey, C.W., Dyment, J., Murton, B.J., Eds.; Geophysical monograph series; AGU: Washington, DC, USA, 2010; Volume 188, pp. 321–367. https://doi.org/10.1029/2008GM000746.
6. Monecke, T.; Petersen, S.; Hannington, M.D. Constraints on water depth of massive sulfide formation: Evidence from modern seafloor hydrothermal systems in arc-related settings. *Econ. Geol.* **2014**, *109*, 2079–2101. https://doi.org/10.2113/econgeo.109.8.2079.
7. Lee, J.; Yang, J.S. Global energy transitions and political systems. *Renew. Sustain. Energy Rev.* **2019**, *115*, 109370. https://doi.org/10.1016/j.rser.2019.109370.
8. Petersen, S.; Kratschell, A.; Augustin, N.; Jamieson, J.; Hein, J.R.; Hannington, M.D. News from the seabed: Geological characteristics and resource potential of deep-sea mineral resources. *Mar. Policy* **2016**, *70*, 175–187. https://doi.org/10.1016/j.marpol.2016.03.012.
9. Månberger, A.; Stenqvist, B. Global metal flows in the renewable energy transition: Exploring the effects of substitutes, technological mix and development. *Energy Policy* **2018**, *119*, 226–241. https://doi.org/10.1016/j.enpol.2018.04.056.
10. Hund, K.; La Porta, D.; Fabregas, T.; Laing, T.; Drexhage, J. *Minerals for Climate Action: The Mineral Intensity of the Clean Energy Transition*; Technical Report; The World Bank Group: Washington, DC, USA, 2020; pp. 1–112. https://doi.org/10.1596/33431.
11. International Energy Agency (IEA). *The Role of Critical Minerals in Clean Energy Transitions*; Technical Report; IEA: Paris, France, 2021; pp. 1–287.
12. Lusty, P.A.J.; Murton, B.J. Deep-ocean mineral deposits: Metal resources and windows into earth processes. *Elements* **2018**, *14*, 301–306. https://doi.org/10.2138/gselements.14.5.301.
13. Savelli, C.; Marani, M.P.; Gamberi, F. Geochemistry of metalliferous, hydrothermal deposits in the Aeolian arc (Tyrrhenian Sea). *J. Volcanol. Geotherm. Res.* **1999**, *88*, 305–323. https://doi.org/10.1016/S0377-0273(99)00007-4.
14. Dekov, V.M.; Savelli, C. Hydrothermal activity in the SE Tyrrhenian Sea: An overview of 30 years of research. *Mar. Geol.* **2004**, *204*, 161–185. https://doi.org/10.1016/S0025-3227(03)00355-4.
15. Gamberi, F.; Savelli, C.; Marani, M.P.; Ligi, M.; Bortoluzzi, G.; Landuzzi, V.; Luppi, A.; Costa, M. Contesto morfo-tettonico e depositi idrotermali di solfuri ed ossidi di ferro in una porzione sommersa dell'Arco Eoliano. *Boll. Soc. Geol. Ital.* **1998**, *117*, 55–71.
16. Becke, R.; Pohl, T.; Ganß, R.; Stanulla, R.; Merkel, B. Chemical and isotopic investigations of submarine fluid discharges from Panarea, Aeolian Islands, Italy. *FOG–Freib. Online Geosci.* **2009**, *21*, 1–180.

17. Stanulla, R.; Pohl, T.; Müller, C.; Merkel, B. Structural and mineralogical study of active and inactive hydrothermal fluid discharges in Panarea, Italy. *Environ. Earth Sci.* **2017**, *76*, 404. https://doi.org/10.1007/s12665-017-6714-6.
18. Dekov, V.M.; Kamenov, G.D.; Abrasheva, M.D.; Capaccioni, B.; Munnik, F. Mineralogical and geochemical investigation of seafloor massive sulfides from Panarea Platform (Aeolian Arc, Tyrrhenian Sea). *Chem. Geol.* **2013**, *335*, 136–148. https://doi.org/10.1016/j.chemgeo.2012.10.048.
19. Marani, M.P.; Gamberi, F.; Savelli, C. Shallow-water polymetallic sulfide deposition in the Aeolian island arc. *Geology* **1997**, *25*, 815–818. https://doi.org/10.1130/0091-7613(1997)025<0815:SWPSDI>2.3.CO;2.
20. Van Dover, C.L.; Ardron, J.A.; Escobar, E.; Gianni, M.; Gjerde, K.M.; Jaeckel, A.; Jones, D.O.B.; Levin, L.A.; Niner, H.J.; Pendleton, L.; et al. Biodiversity loss from deep-sea mining. *Nat. Geosci.* **2017**, *10*, 464–465. https://doi.org/10.1038/ngeo2983.
21. Levin, L.A.; Girguis, P.R.; German, C.R.; Brennan, M.L.; Tüzün, S.; Wagner, J.; Smart, C.; Kruger, A.; Inderbitzen, K.; Le, J.; et al. Exploration and discovery of methane seeps and associated communities in the California Borderland. In *New Frontiers in Ocean Exploration: The E/V Nautilus and NOAA Ship Okeanos Explorer 2015 Field Season*; Bell, K.L.C., Brennan, M.L., Flanders, J., Raineault, N.A., Wagner, K., Eds.; The Oceanography Society: Rockville, MD, USA, 2016; pp. 40–43. https://doi.org/10.5670/oceanog.2016.supplement.01.
22. Thompson, K.F.; Miller, K.A.; Currie, D.; Johnston, P.; Santillo, D. Seabed Mining and Approaches to Governance of the Deep Seabed. *Front. Mar. Sci.* **2018**, *5*, 480. https://doi.org/10.3389/fmars.2018.00480.
23. Miller, K.A.; Thompson, K.F.; Johnston, P.; Santillo, D. An overview of seabed mining including the current state of development, environmental impacts, and knowledge gaps. *Front. Mar. Sci.* **2018**, *4*, 418. https://doi.org/10.3389/fmars.2017.00418.
24. Gabbianelli, G.; Gillot, P.Y.; Lanzafame, G.; Romagnoli, C.; Rossi, P.L. Tectonic and volcanic evolution of Panarea (Aeolian Islands, Italy). *Mar. Geol.* **1990**, *92*, 313–326. https://doi.org/10.1016/0025-3227(90)90011-8.
25. Francalanci, L.; Manetti, P. Geodynamic models of the southern Tyrrhenian region: Constraints from the petrology and geochemistry of the Aeolian volcanic rocks. *Boll. Geof. Teor. Appl.* **1994**, *36*, 283–292. https://doi.org/10.1016/j.earscirev.2006.08.004.
26. Beccaluva, L.; Gabbianelli, G.; Lucchini, F.; Rossi, P.L.; Savelli, C. Petrology and K-Ar ages of volcanics dredged from the Eolian Seamounts; implications for geodynamic evolution of the southern Tyrrhenian basin. *Earth Planet. Sci. Lett.* **1985**, *74*, 187–208. https://doi.org/10.1016/0012-821X(85)90021-4.
27. Kastens, K.; Mascle, J.; Auroux, C. ODP Leg 107 in the Tyrrhenian Sea: Insights into passive margin and back-arc basin evolution. *Geol. Soc. Am. Bull.* **1988**, *100*, 1140–1156. https://doi.org/10.1130/0016-7606(1988)100<1140:OLITTS>2.3.CO;2.
28. Peccerillo, A. *Plio-Quaternary Volcanism in Italy: Petrology, Geochemistry, Geodynamics*; Springer: Berlin/Heidelberg, Germany, 2005; pp. 1–365. https://doi.org/10.1007/3-540-29092-3.
29. Spagnoli, F.; Romeo, T.; Andaloro, F.; Canese, S.; Esposito, V.; Grassi, M.; Biscotti, E.D.; Giordano, P.; Bortoluzzi, G. Seeps and tectonic structure of the hydrothermal system of the Panarea Volcanic Complex (Aeolian Islands, Tyrrhenian Sea). *Geosciences* **2024**, *14*, 60.
30. Calanchi, N.; Capaccioni, B.; Martini, M.; Tassi, F.; Valentini, L. Submarine gas-emission from Panarea Island (Aeolian archipelago): Distribution of inorganic and organic compounds and inferences about source conditions. *Acta Vulcanol.* **1995**, *7*, 43–48.
31. Italiano, F.; Nuccio, P.M. Geochemical investigations of submarine exhalations to the east of Panarea, Aeolian Islands, Italy. *J. Volcanol. Geotherm. Res.* **1991**, *46*, 125–141. https://doi.org/10.1016/0377-0273(91)90079-F.
32. Gugliandolo, C.; Maugeri, T.L. Phylogenetic diversity of archaea in shallow hydrothermal vents of Eolian Islands, Italy. *Diversity* **2019**, *11*, 156. https://doi.org/10.3390/d11090156.
33. Esposito, V.; Andaloro, F.; Canese, S.; Bortoluzzi, G.; Bo, M.; Di Bella, M.; Italiano, F.; Sabatino, G.; Battaglia, P.; Consoli, P.; et al. Exceptional discovery of a shallow-water hydrothermal site in the SW area of Basiluzzo islet (Aeolian archipelago, South Tyrrhenian Sea): An environment to preserve. *PLoS ONE* **2018**, *13*, e0190710. https://doi.org/10.1371/journal.pone.0190710.
34. Di Bella, M.; Sabatino, G.; Ferretti, A.; Quartieri, S.; Cavalazzi, B.; Barbieri, R.; Messori, F.; Italiano, F. Modern iron ooids of hydrothermal origin as a proxy for ancient deposits. *Sci. Rep.* **2019**, *9*, 7107. https://doi.org/10.1038/s41598-019-43181-y.
35. Pichler, T.; Dix, G.R. Hydrothermal venting within a coral reef ecosystem, Ambitle Island, Papua New Guinea. *Geology* **1996**, *24*, 435–438. https://doi.org/10.1130/0091-7613(1996)024%3C0435:HVWACR%3E2.3.CO;2.
36. Prol-Ledesma, R.M.; Canet, C.; Torres-Vera, M.A.; Forrest, M.J.; Armienta, M.A. Vent fluid chemistry in Bahía Concepción coastal submarine hydrothermal system, Baja California Sur, Mexico. *J. Volcanol. Geotherm. Res.* **2004**, *137*, 311–327. https://doi.org/10.1016/j.jvolgeores.2004.06.003.
37. Bortoluzzi, G.; Romeo, T.; La Cono, V.; La Spada, G.; Smedile, F.; Esposito, V.; Sabatino, G.; Di Bella, M.; Canese, S.; Scotti, G.; et al. Ferrous iron- and ammonium-rich diffuse vents support habitat-specific communities in a shallow hydrothermal field off the Basiluzzo Islet (Aeolian Volcanic Archipelago). *Geobiology* **2017**, *15*, 664–677. https://doi.org/10.1111/gbi.12237.

38. Lucchi, F.; Tranne, C.A.; Peccerillo, A.; Keller, J.; Rossi, P.L. Geological history of the Panarea volcanic group (eastern Aeolian archipelago). In *The Aeolian Marine Archipelago: Stratigraphy and Structural Evolution*; Lucchi, F., Peccerillo, A., Keller, J., Tranne, C.A., Rossi, P.L., Eds.; Geological Society London Memoirs; Geological Society of London: London, UK, 2013; Volume 37, pp. 419–455. https://doi.org/10.1144/M37.12.
39. Romano, D.; Caruso, C.; Gattuso, A.; Lazzaro, G.; Longo, M.; Scirè Scappuzzo, S.; Italiano, F. Hazard scenarios related to submarine volcanic-hydrothermal activity and advanced monitoring strategies: A study case from the Panarea Volcanic Group (Aeolian Islands, Italy). *Geofluids* **2019**, *2019*, 8728720. https://doi.org/10.1155/2019/8728720.
40. Caracausi, A.; Ditta, M.; Italiano, F.; Longo, M.; Nuccio, P.M.; Paonita, A.; Rizzo, A. Changes in fluid geochemistry and physico-chemical conditions of geothermal systems caused by magmatic input: The recent abrupt outgassing off the island of Panarea (Aeolian Islands, Italy). *Geochim. Cosmochim. Acta* **2005**, *69*, 3045–3059. https://doi.org/10.1016/j.gca.2005.02.011.
41. Esposito, A.; Giordano, G.; Anzidei, M. The 2002–2003 submarine gas eruption at Panarea volcano (Aeolian Islands, Italy): Volcanology of the seafloor and implications for hazard assessment. *Mar. Geol.* **2006**, *227*, 119–134. https://doi.org/10.1016/j.margeo.2005.11.007.
42. Peccerillo, A.; De Astis, G.; Faraone, D.; Forni, F.; Frezzotti, M. Compositional variations of magmas in the Aeolian arc: Implications for petrogenesis and geodynamics. In *The Aeolian Island Volcanoes*; Lucchi, F., Peccerillo, A., Keller, J., Tranne, C.A., Rossi, P.L., Eds.; Geological Society of London: London, UK, 2013; pp. 491–510. https://doi.org/10.1144/M37.15.
43. Lucchi, F.; Tranne, C.A.; Calanchi, N.; Rossi, P.L. Late Quaternary deformation history of the volcanic edifice of Panarea, Aeolian Arc, Italy. *Bull. Volcanol.* **2007**, *69*, 239–257. https://doi.org/10.1007/s00445-006-0070-9.
44. Pouchou, J.L.; Pichoir, F. Surface film X-ray microanalysis. *Scanning* **1990**, *12*, 212–224. https://doi.org/10.1002/sca.4950120407.
45. Bruker, A.X.S. *Lab Report XRF 90: S8 TIGER–High-Performance Trace Analysis in Geological Samples*; Order No. DOC-L80-E00090; Bruker AXS GmbH: Karlsruhe, Germany, 2007.
46. Bergmann, J.; Friedel, P.; Kleeberg, R. BGMN–a new fundamental parameters based Rietveld program for laboratory X-ray sources; it's use in quantitative analysis and structure investigations. *CPD Newsl.* **1998**, *20*, 5–8.
47. Langford, J.I.; Wilson, A.J.C. Scherrer after Sixty Years: A Survey and Some New Results in the Determination of Crystallite Size. *J. Appl. Crystallogr.* **1978**, *11*, 102–113. https://doi.org/10.1107/S0021889878012844.
48. Taylor, S.R.; Mc Lennan, S.M. The Composition and Evolution of the Continental Crust: Rare Earth Element Evidence from Sedimentary Rocks. *Philos. Trans. R. Soc. A* **1981**, *301*, 381–399. https://doi.org/10.1098/rsta.1981.0119.
49. Large, R.R. Australian volcanic-hosted massive sulfide deposits; recent advances in features and setting. *Econ. Geol.* **1992**, *87*, 471–510. https://doi.org/10.2113/gsecongeo.87.3.471.
50. Hannington, M.D.; de Ronde, C.E.J.; Petersen, S. Sea-floor tectonics and submarine hydrothermal systems. In *Economic Geology 100th Anniversary Volume*; Hedenquist, J.W., Thompson, J.F.H., Goldfarb, R.J., Richards, J.P., Eds.; SEG: Littleton, CO, USA, 2005, pp. 111–141. https://doi.org/10.5382/AV100.06.
51. Cornell, R.M.; Schwertmann, U. *The Iron Oxides: Structure, Properties, Reactions, Occurrences and Uses*, 2nd ed.; Wiley-VCH: Weinheim, Germany, 2003; pp. 1–664. https://doi.org/10.1002/3527602097.
52. Chan, C.S.; Fakra, S.C.; Emerson, D.; Fleming, E.J.; Edwards, K.J. Lithotrophic iron-oxidizing bacteria produce organic stalks to control mineral growth: Implications for biosignature formation. *ISME J.* **2011**, *5*, 717–727. https://doi.org/10.1038/ismej.2010.173.
53. Emerson, D.; Moyer, C.L. Neutrophilic Fe-oxidizing bacteria are abundant at the Loihi Seamount hydrothermal vents and play a major role in Fe oxide deposition. *Appl. Environ. Microbiol.* **2002**, *68*, 3085–3093. https://doi.org/10.1128/AEM.68.6.3085-3093.2002.
54. Swaddle, T.W.; Oltmann, P. Kinetics of the magnetite–maghemite–hematite transformation, with special reference to hydrothermal systems. *Can. J. Chem.* **1980**, *58*, 1773–1779. https://doi.org/10.1139/v80-279.
55. Kristmannsdóttir, H.; Tómasson, J. Zeolite zones in geothermal areas in Iceland. In *Natural Zeolites: Occurrence, Properties, Use*; Sand, L.B., Mumpton, F.A., Eds.; Pergamon Press: Elmsford, NY, USA, 1978; pp. 277–284.
56. Reyes, A.G. Petrology of Philippine geothermal systems and the application of alteration mineralogy to their assessment. *J. Volcanol. Geotherm. Res.* **1990**, *43*, 279–309. https://doi.org/10.1016/0377-0273(90)90057-M.
57. Fulignati, P. Clay Minerals in Hydrothermal Systems. *Minerals* **2020**, *10*, 919. https://doi.org/10.3390/min10100919.
58. Deer, W.A.; Howie, R.A.; Zussman, J. *An Introduction to the Rock-Forming Minerals*, 3rd ed.; Mineralogical Society of Great Britain and Ireland: Twickenham, UK, 2013; pp. 1–510. https://doi.org/10.3749/canmin.51.4.663.

59. Prautsch, A.; Stanulla, R.; Pohl, T.; Merkel, B. Geochemical-mineralogical investigation of degassing structures caused by recent volcanic hydrothermalism, La Calcara, Panarea (Italy). In *3rd International Workshop 'Research in Shallow Marine and Fresh Water Systems'*; Thomas Pichler: Bremen, Germany, 2013.
60. Chipera, S.J.; Bish, D.E. Standardization of X-ray diffraction and chemical analyses of devitrified and vitric tuffs from Yucca Mountain, Nevada. *GSA Annu. Meet.* **2002**, *34*, p. 238.
61. Hannington, M.D.; Scott, S.D. Mineralogy and geochemistry of a hydrothermal silica-sulfide-sulfate spire in the caldera of Axial Seamount, Juan de Fuca Ridge. *Can. Mineral.* **1988**, *26*, 603–625.
62. Hanor, J.S. Barite-celestine geochemistry and environments of formation. *Rev. Mineral. Geochem.* **2000**, *40*, 193–275. https://doi.org/10.2138/rmg.2000.40.4.
63. Griffith, E.M.; Paytan, A. Barite in the ocean–occurrence, geochemistry and palaeoceanographic applications. *Sedimentology* **2012**, *59*, 1817–1835. https://doi.org/10.1111/j.1365-3091.2012.01327.x.
64. Wilkin, R.T.; Barnes, H.L. Formation processes of framboidal pyrite. *Geochim. Cosmochim. Acta* **1997**, *61*, 323–339. https://doi.org/10.1016/s0016-7037(96)00320-1.
65. Rickard, D.; Luther, G.W. Chemistry of iron sulfides. *Chem. Rev.* **2007**, *107*, 514–562. https://doi.org/10.1021/cr0503658.
66. Stoffregen, R.E.; Alpers, C.N. Woodhouseite and svanbergite in hydrothermal ore deposits: Products of apatite destruction during advanced argillic alteration. *Can. Mineral.* **1987**, *25*, 201–211.
67. Hedenquist, J.W.; Arribas, A.R.; Gonzalez-Urien, E. Exploration for epithermal gold deposits. *Rev. Econ. Geol.* **2000**, *13*, 245–277. https://doi.org/10.5382/Rev.13.07.
68. Bigham, J.M.; Schwertmann, U.; Carlson, L.; Murad, E. Schwertmannite and the chemical modeling of iron in acid sulfate waters. *Geochim. Cosmochim. Acta* **1996**, *60*, 2111–2121. https://doi.org/10.1016/0016-7037(96)00091-9.
69. Dill, H.G. The geology of aluminium phosphates and sulphates of the alunite supergroup: A review. *Earth-Sci. Rev.* **2001**, *53*, 35–93. https://doi.org/10.1016/s0012-8252(00)00035-0.
70. Einaudi, M.T.; Hedenquist, J.W.; Inan, E.E. Sulfidation state of fluids in active and extinct hydrothermal systems: Transitions from porphyry to epithermal environments. In *Volcanic, Geothermal, and Ore-Forming Fluids: Rulers and Witnesses of Processes Within the Earth*; Simmons, S.F., Graham, I., Eds.; SEG Special Publication: Littleton, CO, USA, 2003; Volume 10, pp. 285–313. https://doi.org/10.5382/sp.10.15.
71. Velde, B. Composition and mineralogy of clay minerals. In *Origin and Mineralogy of Clays*; Springer: Berlin/Heidelberg, Germany, 1995; pp. 8–42. https://doi.org/10.1007/978-3-662-12648-6_2.
72. Peacock, C.L.; Sherman, D.M. Vanadium(V) adsorption onto goethite at pH to: A surface complexation model based on ab initio molecular geometries and EXAFS spectroscopy. *Geochim. Cosmochim. Acta* **2004**, *68*, 1723–1733. DOI: 10.1016/j.gca.2003.10.018.
73. Dixit, S.; Hering, J.G. Comparison of arsenic(V) and arsenic(III) sorption onto iron oxide minerals: Implications for arsenic mobility. *Environ. Sci. Technol.* **2003**, *37*, 4182–4189. https://doi.org/10.1021/es030309t.
74. Goldberg, T.; Archer, C.; Vance, D.; Poulton, S.W. Mo isotope fractionation during adsorption to Fe (oxyhydr)oxides. *Geochim. Cosmochim. Acta* **2009**, *73*, 6502–6516. https://doi.org/10.1016/j.gca.2009.08.004.
75. Toner, B.M., Marcus, M.A., Edwards, K.J., Rouxel, O., German, C.R. Measuring the Form of Iron in Hydrothermal Plume Particles. Oceanography 2012, 25(1), 209-212. https://doi.org/10.5670/oceanog.2012.19, https://archimer.ifremer.fr/doc/00077/18776/
76. Halbach, P.; Segl, M.; Puteanus, D.; Mangini, A. Co-fluxes and growth rates in ferromanganese deposits from central Pacific seamount areas. *Nature* **1983**, *304*, 716–719. https://doi.org/10.1038/304716a0.
77. Hein, J.R.; Koschinsky, A.; Bau, M.; Manheim, F.T.; Kang, J.K.; Roberts, L. Cobalt-rich ferromanganese crusts in the Pacific. In *Manganese Mineralization: Geochemistry and Mineralogy of Terrestrial and Marine Deposits*; Nicholson, K., Hein, J.R., Bühn, B., Dasgupta, S., Eds.; Geological Society Special Publication: Bath, UK, 1997; Volume 119, pp. 123–138.
78. Gion, A.M., Gaillard, F. The multicomponent exchange of metals between magmatic fluids and silicate melts. *Geochim. Cosmochim. Acta* **2025**, *395*, 112-134. https://doi.org/10.1016/j.gca.2025.01.033
79. Price, R.E.; Pichler, T. Abundance and bioavailability of antimony and arsenic in a marine carbonate aquifer, Florida. *Chem. Geol.* **2006**, *226*, 44–56. https://doi.org/10.1016/j.chemgeo.2005.11.018.
80. Crusius, J.; McKeown, K.; Calvert, S.E.; Pedersen, T.F. Rhenium and molybdenum enrichments in sediments as indicators of oxic, suboxic and sulfidic conditions of deposition. Earth Planet. *Sci. Lett.* **1996**, *145*, 65–78. https://doi.org/10.1016/S0012-821X(96)00204-X.
81. McManus, J.; Berelson, W.M.; Severmann, S.; Poulson, R.L.; Hammond, D.E.; Klinkhammer, G.P.; Holm, C. Molybdenum and uranium geochemistry in continental margin sediments: Paleoproxy implications. *Geochim. Cosmochim. Acta* **2006**, *70*, 4643–4662. https://doi.org/10.1016/j.gca.2006.06.1564.

82. Halbach, P.; Pracejus, B.; Marten, A. Geology and mineralogy of seafloor hydrothermal oxides and sulfides in the Okinawa Trough–a review. *Oceanol. Acta* **1993**, *16*, 501–521. https://doi.org/10.2113/gsecongeo.88.8.2210.
83. Gamo, T.; Okamura, K.; Charlou, J.L.; Urabe, T.; Auzende, J.M.; Ishibashi, J.; Shitashima, K.; Chiba, H. Shipboard Scientific Party of the ManusFlux Cruise, Acidic and sulfate-rich hydrothermal fluids from the Manus back-arc basin, Papua New Guinea. *Geology* **1997**, *25*, 139–142. https://doi.org/10.1130/0091-7613(1997)025<0139:AASRHF>2.3.CO;2.
84. Dando, P.R.; Hughes, J.A.; Leahy, Y.; Niven, S.J.; Taylor, L.J.; Smith, P.R. Gas venting rates from submarine hydrothermal areas around the island of Milos, Hellenic Volcanic Arc. *Cont. Shelf Res.* **1995**, *15*, 913–929. https://doi.org/10.1016/0278-4343(95)80002-U.
85. Price, R.E.; Lesniewski, R.; Nitzsche, K.S.; Meyerdierks, A.; Saltikov, C.; Pichler, T.; Amend, J.P. Archaeal and bacterial diversity in an arsenic-rich shallow-sea hydrothermal system undergoing phase separation. *Front. Microbiol.* **2013**, *4*, 158. https://doi.org/10.3389/fmicb.2013.00158.
86. Pichler, T.; Veizer, J. Precipitation of Fe(III) oxyhydroxide deposits from shallow-water hydrothermal fluids in Tutum Bay, Ambitle Island, Papua New Guinea. *Chem. Geol.* **1999**, *162*, 15–31. https://doi.org/10.1016/S0009-2541(99)00068-6.
87. Hekinian, R.; Hoffert, M.; Larque, P.; Cheminee, J.L.; Stoffers, P.; Bideau, D. Hydrothermal Fe and Si oxyhydroxide deposits from South Pacific intraplate volcanoes and East Pacific Rise axial and off-axial regions. *Econ. Geol.* **1993**, *88*, 2099–2121. https://doi.org/10.2113/gsecongeo.88.8.2099.
88. Boyd, T.; Scott, S.D.; Hekinian, R. Trace element patterns in Fe–Si–Mn oxyhydoxides at three hydrothermal active seafloor regions. *Res. Geol.* **1993**, *17*, 83–95.
89. Marini, L.; Vespasiano, G.; De Rosa, R.; Viccaro, M.; Principe, C.; Bloise, A.; Fuoco, I.; Lelli, M.; La Russa, M.F.; Caruso, C.G.; et al. The geothermal resources of Vulcano Island (Aeolian archipelago, Italy). *Renew. Energy* **2025**, *253*, 123622. https://doi.org/10.1016/j.renene.2025.123622.
90. Floridia, G.; Viccaro, M. Geological field investigation for the assessment of the low-grade geothermal resources from volcanic terrains of the Island of Salina (Aeolian Islands, Italy). *IOP Conf. Ser. Earth Environ. Sci.* **2019**, *367*, 012007. https://doi.org/10.1088/1755-1315/367/1/012007.
91. Jørgensen, B.B.; Kasten, S. Sulfur cycling and methane oxidation. In *Marine Geochemistry*; Schulz, H.D., Zabel, M., Eds.; Springer: Berlin/Heidelberg, Germany, 2006, 271–309.